Ph.D Thesis

Direct and indirect transitions of angle-resolved photoemssion spectroscopy in graphene and graphite

Department of Physics

Graduate School of Science, Tohoku University

Pourya Ayria

2016

Acknowledgments

Since I was a child I had a dream and now I am here to fulfill my childhood dream and I am writing to tell thank you to whom help me as a human being to achieve my dream.

When I was in my country I met a researcher come from Japan in a workshop who has had an undeniable impact on my decision to come Japan. He shared a part of his life with me by telling me his life story. He was working as a cook and his mother was a Japanese dancer, one day, when he was listening to a radio program everything changed because he heard a magic sentence from the radio that was 'if you make a decision and try to accomplish it you can change your life'. Then, he started to study physics and finally he became a physicist. I was so impressed about his story and Japan, how people can improve their life in Japan. Thus, after finishing my master, although I had a chance to continue my education in other countries I decided to go Japan.

Since I was studying during master, I read many chapters of my academic bible, "properties of carbon nanotubes" written by professors *Saito*, G. and M. dresslhaus and their papers about carbon nanotubes. It was my motivation to send an email to professor *Saito*. He replied the email and the chapter of my life in Japan started. He accepted my conditions to submit my application for the MEXT scholarship. Thanks to Japanese government that provide opportunities for students all around the world to study in Japan and have experience about Japanese cultures. I participated in the entrance examination and passed it and by the support of professor *Saito* I could get the scholarship and join his lab. I would like to appreciate professor *Saito* to support me to get this position. Then, I met another Japanese person who affected on my life, professor Shinichiro Tanaka, in my first conference in Japan. He is so kind, supportive and humble person. I learned many things about ARPES from him; and, with no doubt, I can write this thesis because of the collaboration with him. I would like to appreciate professor *Saito* again for giving me a chance to discuss and collaborate with professor M. Dresselhaus when she came to Japan. After I met her, I understood why she is called "Queen" not only for carbon but also as a scientist.

In Japan, my life has many ups and downs, I found two brothers, one from Indonesia, Siregar, and the other one from Brasil, Thomas. I lived with Siregar for one year and half

in the same unit of dormitory. When I was depressed and tired, he always kindly listened to me and gave me some advice. He taught me many things about Indonesia. Thomas, he is my best friend in Japan, my neighbor and collaborator. Nowadays, we are the intimate friend that sometimes we can understand each other just by looking each other. This kind of friendship will last forever. We had many discussions about group theory together. So long story short, if I want to appreciate Thomas I need to write another thesis. Thomas and Siregar emotionally supported me a lot when my father passed away and I did not have a chance to go back to my country and say my last good bye to my father who has taught not only me but also his students many lessons about the life. He taught me 'sharing happiness brings more happiness' and 'nobody can build a house by destroying others house'. I would like to appreciate my mother who support me all seconds of my life, as well as my older sister who is always more worried about my life than me. I hope one day I can make up their kindness.

I would like to appreciate Dr. Nugraha, particularly for accompanying me at weekly discussion in my last semester and for helping me to write my papers. I am really thankful Hesky san to help me in my presentations. I want to say thanks to Inoue and Shirakura san for teaching me many things about Japanese culture and for doing sport together. I was very lucky to meet, Hung, he is a master of Quantum Espresso and I learned many things from him. I would like appreciate Wako san and Sato san who always helped me to fill in my documents and to do my printing job in Tohoku University. I appreciate all friends who I cannot mention their name and our stories here.

All and all some people come to our life and help us to achieve our dream and some people block it; but this is the life, and we need to "頑張って" . I hope that all things that happened during my life in Japan will help me to become more mature, decent and knowledgeable person in my life.

Contents

Chapter 1

Introduction

1.1 Purpose of the study

In the last decade, graphene and graphene-based atomic layer materials have provided us with intensive nanoscale research in terms of their novel electronic structures and advanced applications [1, 2, 3, 4, 5]. In order to understand various phenomena in these materials, it is necessary for us to study their electronic structure and vibrational properties of graphene based-materials. With this regard, angle-resolved photoemission spectroscopy (ARPES) is a useful method to explore electronic properties of solids. In ARPES, if the energy of photo-excited electrons surpasses the work function of the sample, the photoelectrons are ejected from the surface of a material. The kinetic energy and momentum of the photoelectron are observed by an analyzer from which we can directly get information on the electron in solids [6]. In this thesis, we will study the direct and indirect ARPES spectra near the K and Γ points, respectively, of Brillouin zone of graphene and graphite, by means of the different photon energies and light polarizations and discuss how significantly different physics from these regions are. Therefor, **The purpose of this thesis**, is to answer follows questions in details:

Direct transition:

1) What is the photon energy dependence of ARPES spectra in graphene?

2) What is the polarization dependence of ARPES spectra in graphene?

Indirect transition:

1) How the phonon dispersion relations of the graphene and graphite can be observed by the observation of the indirect transition ARPES spectra?

2) Which phonon mode can be observed by the ARPES?

3) What is the photon dependence of the indirect transition ?

4) What is the polarization dependence of indirect transition ?

The rest of this thesis is going to answer mentioned questions step-by-step. The study of ARPES spectra near the K point and closed to the Fermi level enable us to determine the optical properties of the the π and π^* bands. The dependence of the ARPES intensity on the energy and polarization of an incident light play important roles to resolve the ARPES intensity because the ARPES intensity critically changes by modifying them [7, 8, 9, 10]. Changing the photon energy is assisted to determine features of the unoccupied states in graphene and graphite. The polarization of the incident light help us to analyze the symmetry selection rule for the direct and indirect transitions. Therefore, by symmetry analysis, we understand the allowed and forbidden transitions. Furthermore, the investigation of ARPES intensity from different wave vectors, particularly, around the Γ point, near to the Fermi level, in graphene and graphite, is also important because the electronic and vibrational properties in graphene and graphite can be obtained through the indirect transitions. For example, it is known that the ARPES spectra around the Γ point and near the Fermi level do not exist for the direct transition; however, there is a possibility an electrons is scattered from near the K point into near the Γ point through the indirect transition, included electron-phonon coupling and electron-photon interaction. Thus, the measurement of the energy and momentum of the scattered electron near the Γ point and near the Fermi level also provide valuable information about the electron-phonon coupling [11, 12].

In this thesis, to understand and to predict theoretically the electronic and vibrational properties of graphene and graphite by the means of ARPES technique near the K and Γ points and close to the Fermi level, we use group theory as well as computational calculation, based on first principles calculations, to explore the photon and polarization dependence of the direct and indirect transition ARPES spectra.

1.2 Organization of the thesis

The present thesis is organized as follows: In the remaining part of Chapter 1, the background for understanding the ARPES is described. In Chapter 2, the fundamentals of graphene an graphite are reviewed, particularly, regarding the geometrical structure, electronic properties, and vibrational properties. The electronic structure and vibrational properties are computed by Quantum Espresso package. In Chapter 3, we show the formulation of the direct transition, includes the electron-photon interaction and the indirect transition, includes the electron-photon interaction and the electron-phonon coupling, in ARPES. Besides, in this Chapter, we proceed the previous formulation of the electron-phonon coupling based on plane wave expansion to obtain a new (original) analytic formulation. The main (original) results of this thesis are presented in Chapter 4, 5 and 6. In Chapter 4, we will discuss about the symmetry transition rules for the direct and indirect transition in graphene and graphite[13]. In Chapter 5, we show photon energy dependence of the ARPES intensity in graphene[13]. In Chapter 6, we show how phonon-assisted indirect transition in ARPES for graphene and graphite. Finally, in Chapter 7, a summery of this thesis is given.

1.3 General backgrounds

Hereafter, in this chapter, we briefly discuss some general concepts that is important to understand ARPES as well as introduce some recent experimental results related to this thesis.

1.3.1 Basics of Photoemission

Electrons and photons are the most easily available particles with which to prob matters. Hence, many spectroscopes technique engage the use of these two types of particles [15]. In a typical spectroscopic experiment an electron or a photon in a more or less well-defined state (energy, direction of propagation, polarization) impinges on a sample. As a result the impact, electrons and/or photons escape from the sample; and, then, the escaping particles are analyzed with a spectrometer. In photoemission spectroscopy (PES), photons are incoming

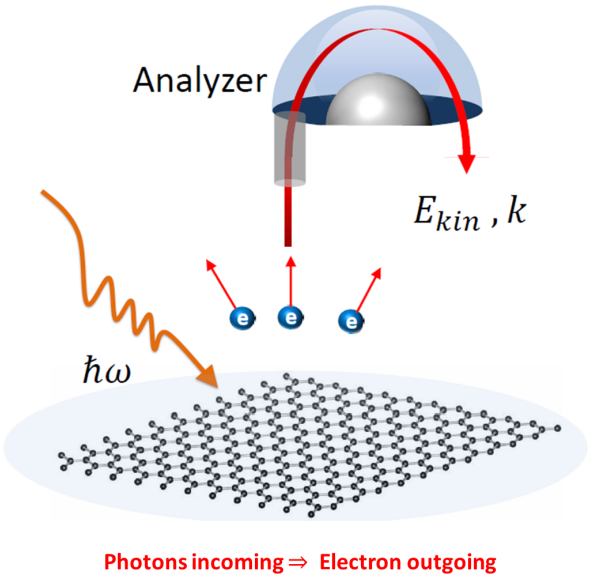

Figure 1-1: In photoemission process, photons are incoming and electrons outgoing. The kinetic energy of photoelectrons are measured.

and electrons, the outgoing particles to be analyzed (see Fig. 1-1). In the most cases in solid, the photoemission process can be roughly modeled by the "three-step model". The three step-model is schematically shown in Fig. 1-2. In this model, it is assumed that the photoemission process can be divided into three steps:

1) The excitation of an electron by an incident photon (creation of a photoelectron),

2) Travel of the photoelectron to the sample surface,

3) Emission of the photoelectron into the vacuum by overcoming the surface potential.

Then, the photoemission intensity as a function of the photoelectron kinetic energy in vacuum E_k and the excitation photon energy $\hbar\omega$ is proportional to the product of the probabilities corresponding to each step [16]. The probabilities of the three-step model are represented by

$$P(E_k, \hbar\omega)T(E_k, \hbar\omega)D(E_k), \tag{1.1}$$

The information on the electronic states of solids is included in the first term. In step (1), the electron is initially excited from an occupied state by the absorption of a photon into an unoccupied state. The photoexcitation probability is explained by the Fermi golden rule[17]

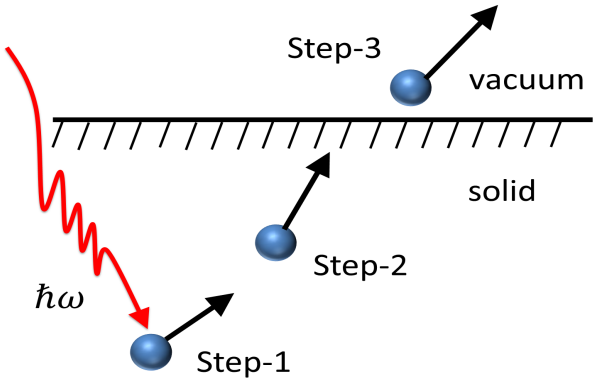

Figure 1-2: (a) Schematic representation of a photoemission process in the three-steps model.(b) Step (1) is the excitation of an electron by an incident photon; step (2) is travel of the photoelectron to the sample surface; step (3) is emission of the photoelectron into the vacuum by overcoming the surface potential [14].

Step (2) can be described in term of represents the probability of the photoelectron motion to the surface without serious inelastic scattering. This process can be expressed by using the absorption coefficient $\alpha(\hbar\omega)$ for the incident photon and the photoelectron inelastic mean free path $\lambda_{mp}(E_k)$. $1/\alpha(\hbar\omega)$ is of the order of 100–1000 Å or more for $\hbar\omega$ in the range of 6–10000 eV which is much longer than $\lambda_{mp}(E_k) \leq 100$ Å for the most element solids as shown in Fig.1-3 [19, 18]. The $T(E_k, \hbar\omega)$ is given as

$$T(E_k, \hbar\omega) = \frac{\alpha(\hbar\omega)\lambda_{mp}(E_k)}{1 + \alpha(\hbar\omega)\lambda_{mp}(E_k)} \simeq \alpha(\hbar\omega)\lambda_{mp}(E_k). \tag{1.2}$$

The λ_{mp} takes a minimum of 3–5 Å at E_k of $15 - 200$ eV in many cases. This minimum length corresponds roughly to lattice constants of various solids. Therefore, the valence-band photoemission spectra with of 15-200 eV by using a He discharge lamp or synchrotron light source mainly reflect the surface electronic states of solid. Step (3), escaping from the bulk, is the final step of the photoemission process. This process can be calculate when the photoelectrons can be treated as nearly free electrons with a potential of depth $E_v - E_0 \equiv V_0$ (this is called the inner potential), where E_v denotes the vacuum level and E_0 stands for the bottom energy in a nearly free electron band. This approximation is appropriate since the photoelectron energy is much higher than that for bound electrons in solids. In the nearly free electron model, the kinetic energy of photoelectron inside the solid is $E_k + V_0$ whereas it

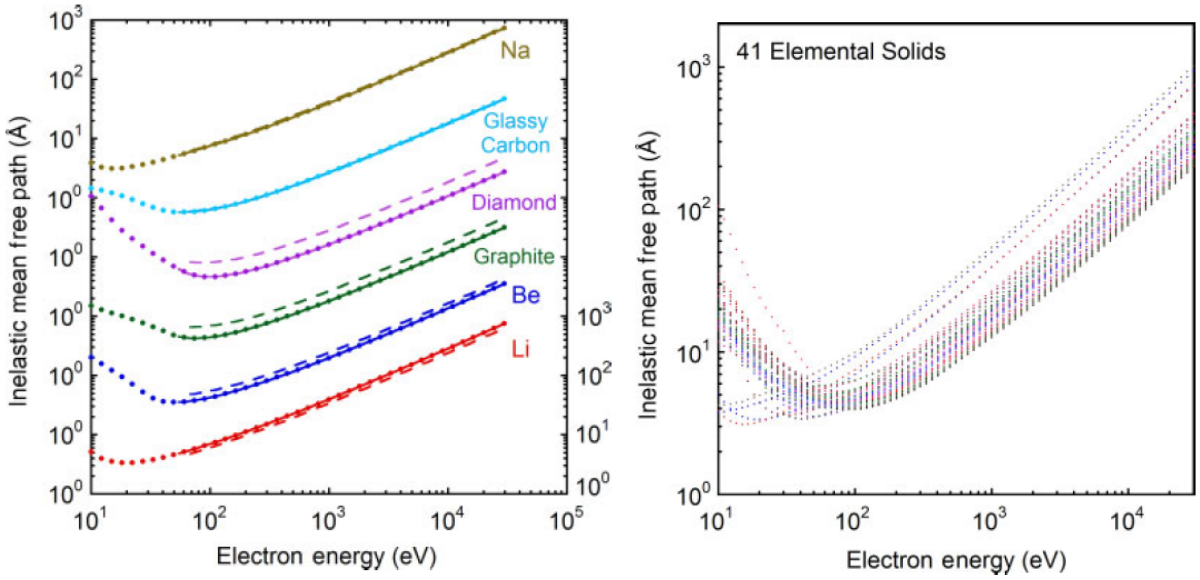

Figure 1-3: (a) Kinetic energy dependence of the photoelectron inelastic mean free path λ_{mp} as a function of electron energy [18]. for (a) several solids (b) 41 elements solids.

becomes E_k suddenly at the boundary. Since the "force" is applied to the photoelectron only perpendicular to the surface, the photoelectron momentum parallel to the sample surface is conserved on the emission into vacuum, which is one of the fundamental principle for ARPES. To satisfy the condition that the perpendicular momentum component of the photoelectron emitted into the vacuum to be possible, $D(E_k)$ is calculated [16] as

$$D(E_k) = \frac{1}{2}\Big(1 - \sqrt{\frac{V_0}{E_k + V_0}}\Big). \tag{1.3}$$

This function depends gently on E_k, and can be regarded as a constant when the recorded kinetic energy range is narrow enough compared with E_k. Therefore, it is hereafter assumed that the E_k dependence on the terms $T(E_k, \hbar\omega)$ and $D_k(E_k)$ is negligible within the discussed kinetic energy rage of one spectrum.

Then, electrons that overcome a solid potential, or work function, ϕ can escape from surface. The work function is define the difference between the material's Fermi level, and the energy level of the vacuum. Fig. 1-4 shows schematically how the energy-level diagram and the energy distribution of photoemitted electrons related to each other. The solid sample has core levels and a valence band. In the the present case of a metal, the Fermi energy

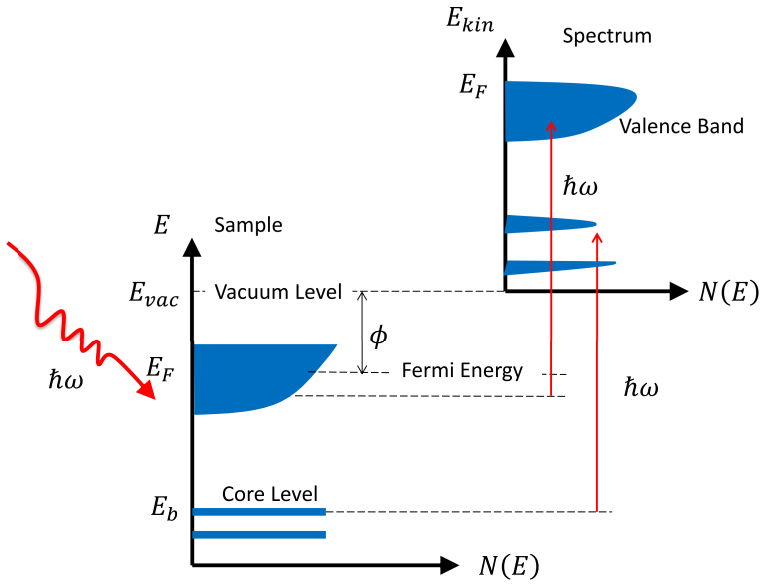

Figure 1-4: The electron energy distribution, $N(E)$, are produced for valence band or core levels by the incoming photons and measured as a function of kinetic energy E_{kin} is expressed in terms of the binding energy E_b, work function ϕ and photon energy $\hbar\omega$. The natural abscissa for the photoelectrons is the kinetic energy with its zero at the vacuum level of the sample ($E_k = \hbar\omega - |E_b| - \phi$) [14].

E_f is at the top of the valence band and has a separation ϕ from the vacuum level E_v [14]. Thus, the kinetic energy of the photoelectron in vacuum can be written as

$$E_k = \hbar\omega - |E_b| - \phi, \tag{1.4}$$

where, E_b, is the so-called binding energy if electrons, which in solids is generally referred to the Fermi level and in free atoms or molecules to the vacuum level. The work function ϕ has a substantial effect on the energy of observed electrons; but, it is common to omit it when reporting photoemission result.

1.3.2 Angle Resolved photoemission Spectroscopy

Angle resolved photoemission spectroscopy is a kind of photoemission spectroscopy. The PES measures only the energy of electrons. ARPES measures not only the energy of electrons, but also their momentum. In this way, ARPES is a direct method to observe the band structure of solids experimentally. Figure 1-5 shows ARPES intensity as function of the

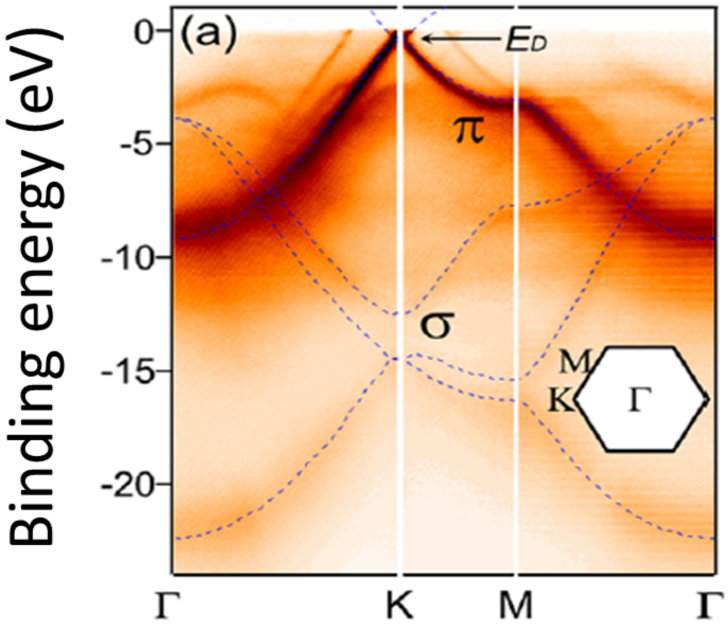

Figure 1-5: The ARPES intensity shows the electron dispersion of graphene along high symmetry point of graphene for $\hbar\omega = 100$ eV [3].

binding energy along the high symmetry point of graphene for the $\hbar\omega = 100$ eV. The π and σ bands of graphene can be seen from this measurement.

The key to understand ARPES is how the momentum of the electron in the vacuum is related to the momentum in the solid. In ARPES, the photoelectron momentum parallel to the sample surface is conserved on the emission into vacuum. As shown in Fig. 1-6, the photoelectron momentum $\mathbf{k}_f$ is the sum of the momentum of electron in the initial state $\mathbf{k}_i$ and the incident photon $\mathbf{q}$, in the reduce zone scheme [14], as

$$k_{f\parallel} = k_{i\parallel} + q_{\parallel}, \tag{1.5}$$

here, the photon momentum normal to the sample surface is defined as $-q_{\perp}$. We can write the momentum in terms of $\mathbf{k}_f$ and the kinetic of the energy, E_k, in vacuum

$$E_k = \frac{\hbar^2 \mathbf{k}_f^2}{2m_e}, \tag{1.6}$$

where m_e is the electron mass. Hence, the parallel wave vector of the photoelectron can be

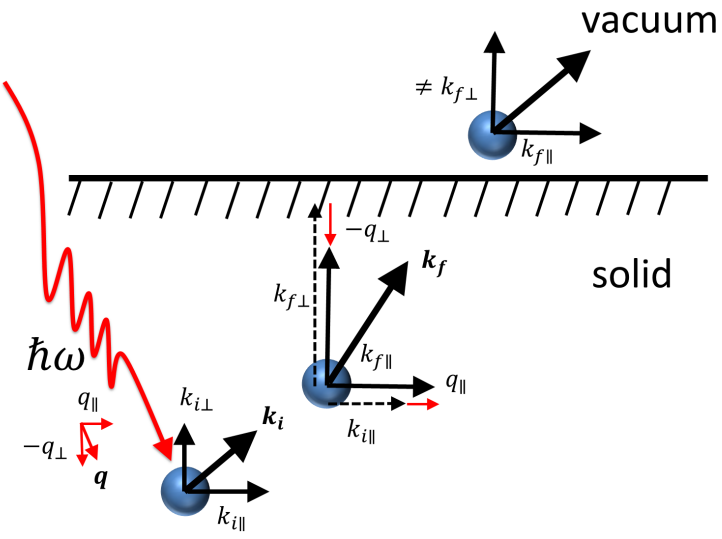

Figure 1-6: Schematic representation of the momentum conservation at each step in the photoemission process in solids. In the figure, photon momentum normal to sample surface is defined as $-q_\perp$ [16].

written as

$$\begin{aligned} k_{f\parallel} &\simeq 0.5\text{Å}^{-1} \sin\theta \sqrt{E_k^V(eV)}, \\ \Delta k_{f\parallel} &\simeq 0.5\text{Å}^{-1} \cos\theta \sqrt{E_k^V(eV)} \Delta\theta. \end{aligned} \tag{1.7}$$

The momentum resolution is obtained as

$$\Delta k_{f\parallel} = \frac{\sqrt{2m_e E_k}}{2\hbar} \cdot \frac{\Delta E_k}{E_k} \sin\theta + \frac{\sqrt{2m_e E_k}}{\hbar} \cos\theta \cdot \Delta\theta. \tag{1.8}$$

where ΔE_k denotes the energy resolution and $\Delta\theta$ stands for the acceptance angle of photoelectrons. In Eq. (1.8), the first term on the right side is negligibly smaller than the second term in general. Recently, typical $\Delta\theta$ is $2^\circ = 0.035$ radiant or larger. If one assumes that the angular acceptance of the electron analyzer is $\Delta\theta = 2^\circ$ and that the detected electrons are photoexcited at the Fermi energy, one has:

$$\Delta k_{f\parallel} = 0.17\text{Å}^{-1}. \tag{1.9}$$

If the $k_{f\parallel}$ is compared with the Brillouin zone dimension of graphite $2\pi/a \simeq 2.55\text{Å}^{-1}$, where

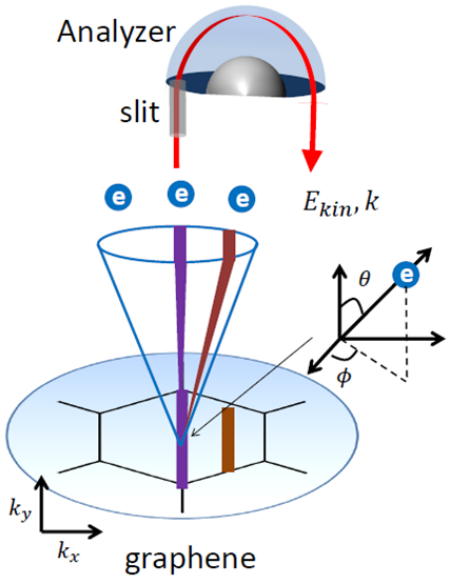

Figure 1-7: Electrons are kicked out from sample with various momentum. Only electrons exciting sample parallel to the slit (purple) will be measured. To observe a different k_x, the brown line, the sample and its corresponding emission cone are rotated until it aligns with slit [21].

$a = 2.46\text{Å}^{-1}$ is graphite lattice parameter, we can find out that the photon wave vector can be neglected. Hence, From Eq. 1.5 and Eq. 1.13

$$k_{i\parallel} = \frac{\sqrt{2mE_k^V}}{\hbar}\sin\theta - q_{\parallel}. \tag{1.10}$$

Although the momentum is not conserved along the surface normal direction, $K_{i\perp}$, it can be obtained when photoelectrons can be treated as nearly free electrons in the solid by using the inner potential V_0 and Eq. 1.5 as

$$k_{i\perp} = \frac{\sqrt{2mE_k^V\cos^2\theta + V_0}}{\hbar} + q_{\perp}. \tag{1.11}$$

The momentum resolution along the normal direction $\Delta k_{f\perp}$ is not determined from Eq. 1.11 but depends on the λ_{mp} [20, 16] as

$$\Delta k_{f\perp} \sim \frac{1}{\lambda_{mp}}. \tag{1.12}$$

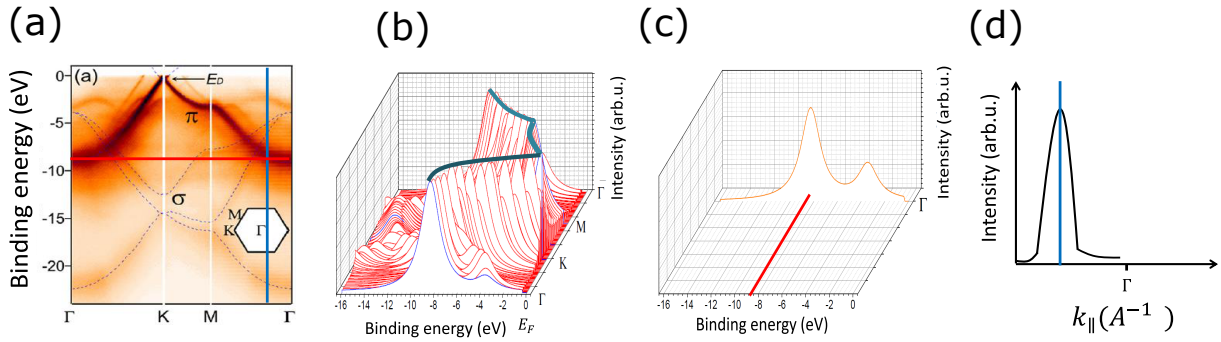

Figure 1-8: (a) The photoemission intensity map of graphene is shown [3]. (b) The schematic raw data that construct the map of graphene band structure. (c) Energy density curve near the Γ point along M–Γ. (d) the momentum density from this data can be extracted.

Moreover, The two parallel components of the wave vector, shown in Fig. 1-7, can be also expressed as:

$$k_{fx} = \frac{\sqrt{2m_e E_k^V}}{\hbar} \sin\theta \cos\phi,$$
$$k_{fy} = \frac{\sqrt{2m_e E_k^V}}{\hbar} \sin\theta \sin\phi, \tag{1.13}$$

θ and ϕ are the angle describing the trajectory of the electron .

To understand how the ARPES measurement maps the electron dispersion of solid, we discuss each step of the measurement separately. Figure 1-8(a) shows the ARPES intensity as a function of the binding energy in graphene along high symmetry point. The electrons escaped from the sample it is detected in an analyzer through a slit parallel to $\phi = 0$. This measurement limits the observation of the electrons with $k_y = 0$ [21]. However, there are possibilities that electrons with various θ, the k_x spectrum, enter the analyzer. Thus, collecting ARPES spectra from different wave vectors map the ARPES spectra which are aligns to the analyzer. For example, data collected from ARPES measurement at a given k_y maybe seen as "slices". The raw data for a slice is shown schematically in Fig. 1-8(b) schematically. For a constant energy and momentum, it is referred to as energy dispersion curves (EDC) Fig. 1-8(c) or momentum dispersion curves (MDC) Fig. 1-8(d). Peaks either of these curves correspond to high photoelectron density, indicating the center of electron band. By combining a series of slices, it is possible to construct a matrix of intensity data spanning the entire Brillouin zone, which varies as a function of momentum k_x and k_y, and

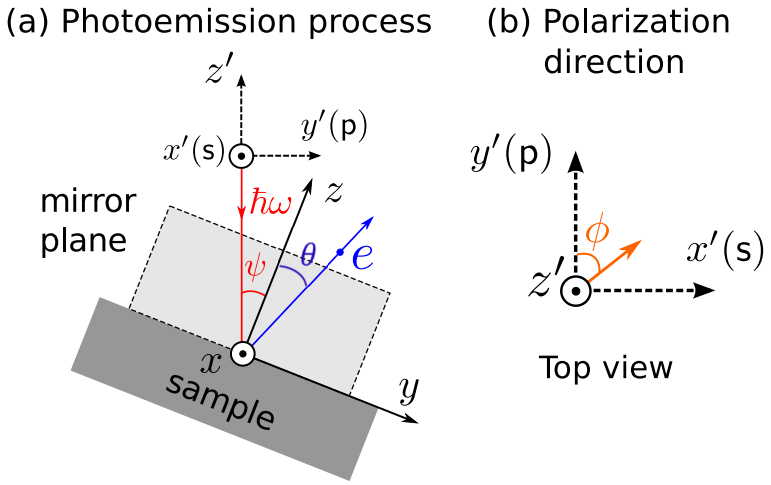

Figure 1-9: (a) Geometry of the photoemission process [13]. The incident photon with energy $\hbar\omega$ are shown by an arrow going to the graphene plane. We can define a mirror plane which contains the directions of the incident light (z' axis), the electrons ejected from the surface, and an axis (z-axis) normal to the graphene surface. The angle between incident light, the ejected electron, and the z-axis is denoted by ψ, θ. (b) Viewing the set-up from the z' axis, the light polarization angle, ϕ, is in the $x'y'$-plane and measured with respect to the y' axis. Here, $\phi = 0°$ and $\phi = 90°$ correspond to the p- and s-polarization, respectively.

binding energy E_b [21]. One common way to represent this data is as a band map. Here, an EDC or combination of several EDC is taken for each k_y. By plotting these in series, it is possible to observe the peak shift in each on. Connecting these peak points , we are able to track the bands across key cut such as $\Gamma - K$ or $\Gamma - M$ in the Brillouin zone.

1.4 Photon and polarization dependence of the ARPES in graphene

The electron energy band structure of graphene can be observed by applying different light polarizations. When the incident light polarization is parallel or perpendicular to a plane that includes the incident light and ejected photoexcited electron, they are named as p-polarized or s-polarized light, respectively [22] (see Fig. 1-9 (a)). Some previous studies showed that, in the ARPES spectra of graphene, π and π^* bands near Dirac point along the Γ–K direction are brightened by the p- and s-polarized light, respectively [7, 8, 9, 10](see Fig. 1-10 (a)). On the other hand, for the direction along K–M, the π and π^* bands, are

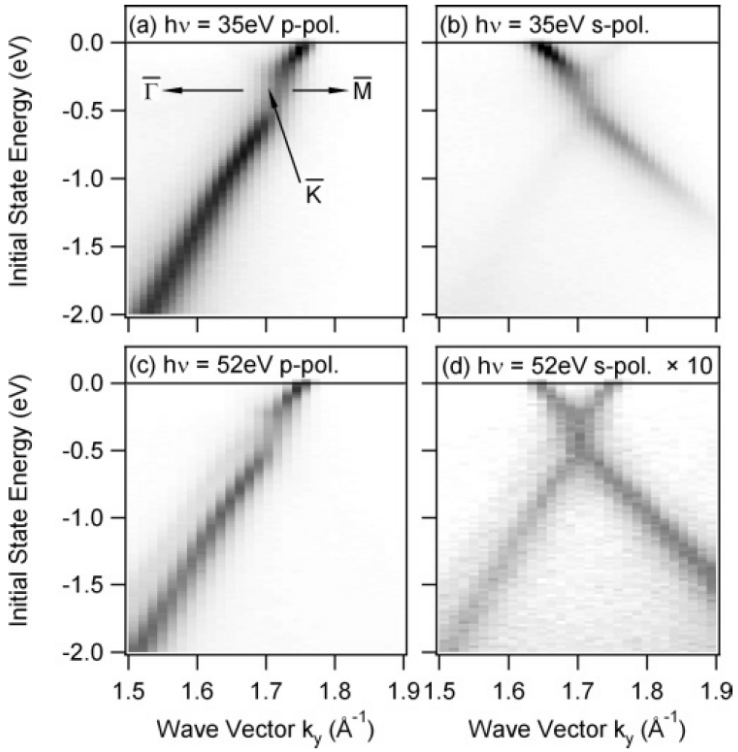

Figure 1-10: Band structure measured along Γ–K for an epitaxial graphene monolayer on SiC(0001) for two different photon energies ((a), (b): $\hbar\omega = 35$ eV; (c), (d): $\hbar\omega = 35$ eV) for (a) p-polarized light (b) s-polarized light. The gray scale is linear with black (white) corresponding to high (low) photoemission intensities [10].

brightened by the s- and p-polarized light, respectively, (see Fig. 1-10 (b)). The energy band brightened by the p-polarized light is referred to as the p-branch, while that brightened by the s-polarized light is called the s-branch. Such polarization dependence is known as the electronic chirality or chiral phenomenon of graphene in ARPES spectra. Fig. 1-11 shows the corresponding Fermi surface around the K point for $\hbar\omega = 35$ eV and $\hbar\omega = 52$ eV with both p- and s- polarized light. For p-polarized radiation Fig. 1-11 (a), there is no photoemission intensity as spot 1. This situation changes drastically when using s-polarized light Fig. 1-11 (b)[10].

Some researchers in the previous studies explained the chiral phenomenon in graphene by considering the interference of electron wave functions for A and B atoms in the initial states [7, 8, 9]. They calculated the electron-photon matrix elements in the presence of p- or s-polarized light for the ARPES intensity and they considered the wave functions of the final states as a single plane wave which has even symmetry with respect to the plane of incident

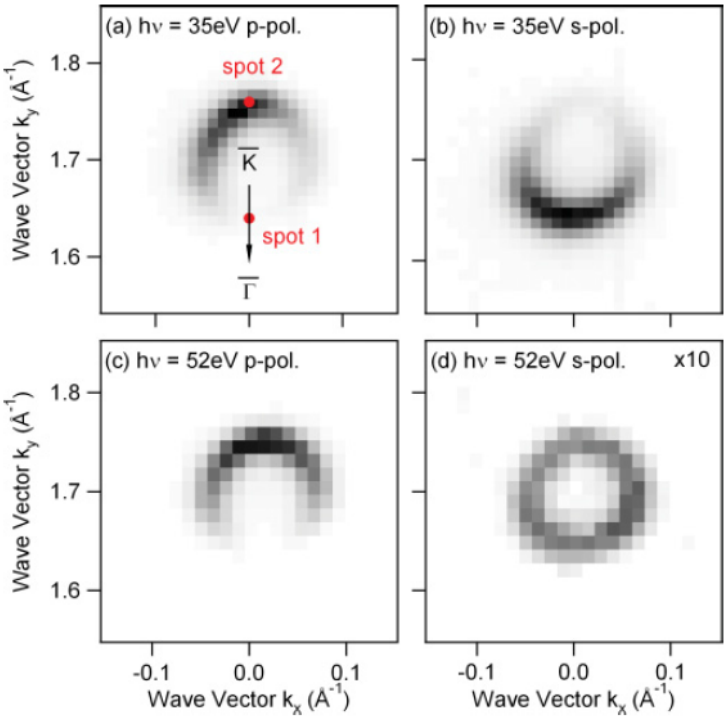

Figure 1-11: Fermi surface of expitaxial graphene on SiC(0001) measured with p-polarized light ((a)-(c)) and s-polarized light ((b),(d)) for different photon energies ((a),(b): $\hbar\omega$ = 35 eV and (c),(d): $\hbar\omega = 52$ eV) [10].

light and ejected electron. Since the dependence of the electron-photon matrix elements on the final state wave functions was not considered to explain the chiral phenomenon, they refer to the phenomenon only as the initial state effects on the electron-photon matrix elements. However, Gruneis *et al.* showed much earlier that, in the calculation of $\pi - \pi^*$ optical transition, the direction of the electron-photon dipole vectors critically depend on the final states [23]. In particular, the direction of the dipole vectors will change for different final states which are independent of light polarization. Thus, studying the final state effects on the electron-photon matrix elements is essential for ARPES spectra.

To consider the final state effects experimentally, we can apply a variation in the photon energy. Gierz *et al.* showed that, by applying different photon energies in ARPES measurement of graphene, the s-polarized light with energy of around 52 eV can illuminate both bands in the direction of Γ–K and K–M due to the change of the final states [25, 10]; their experimental measurement is shown in Fig. 1-5 (c) and (d). Therefore, the whole Fermi surface is illuminate by the s-polarized light (see Fig. 1.6 (d)).

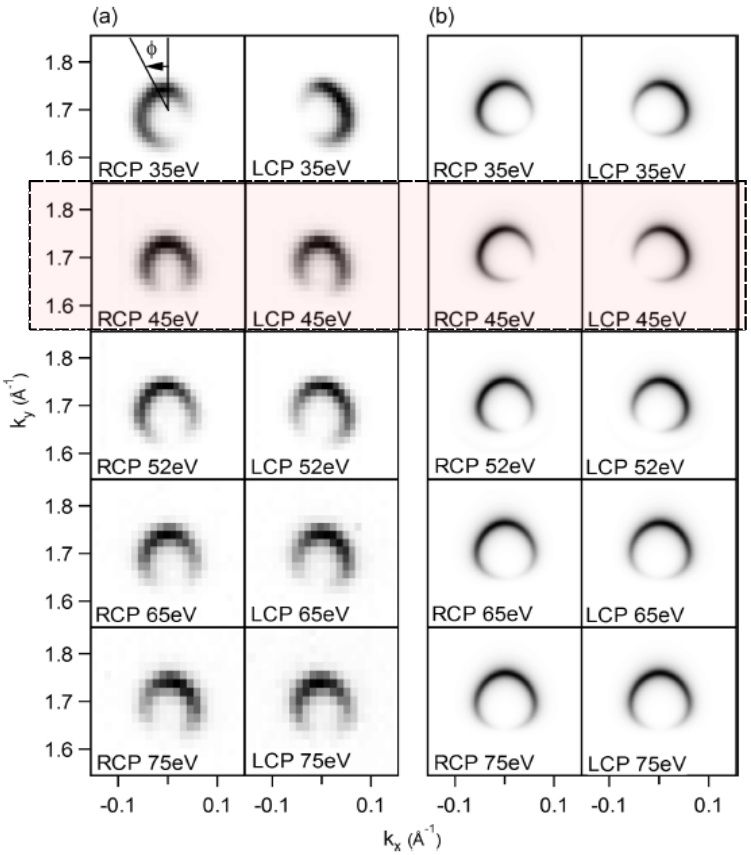

Figure 1-12: Measured (a) and calculated (b) Fermi surface for right circular polarization light (b) left circular polarization light for different photon energies [24]. There is a discrepancy between experimental measurement and calculation for $\hbar\omega = 45$ eV

Furthermore, they used circularly polarized light to observe polarization dependence of ARPES spectra for different photon energy [24]. Their experimental results show that the ARPES intensity for left and right circular polarization becomes almost the same near 46 eV photon energy. However, their theoretical approach did not reproduce the experimental results [24].

Motivated by the above mentioned issues, in this thesis, as the first investigation subject, we combine experimental and theoretical approaches to clarify the photon energy and polarization dependence of ARPES spectra in graphene.

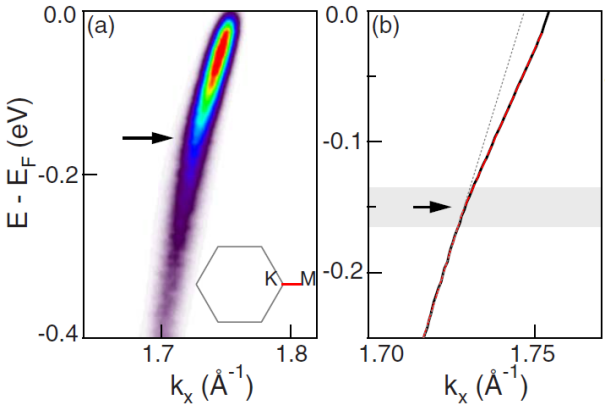

Figure 1-13: (a) ARPES data taken along K–M direction (solid line in the inset). (b) Dispersion (black curve) extracted by fitting the raw data. The dashed line is the fit using two straight line with different slopes. Within 20 meV below E_f, the dispersion is effect by the resolution, and therefore, they fit the dispersion only in the range between -250 and 20 meV. The gray dotted line is a guide for the deviation of the low-energy dispersion from the extrapolation of high-energy dispersion[26].

1.5 An investigation of electron-phonon coupling via phonon dispersion

ARPES is one of the well-established methods to probe the electron-phonon coupling (EPC) in solids [6]. The renormalization of the electronic energy and state due to the EPC have been vastly explored by the observation of the electron dispersion relation near the Dirac point (the K or K' point) in graphene [27, 28, 29]. The EPC renormalization causes appearance of a kink structure in the electron dispersion relation. The ARPES intensity is expressed in terms of the complex self-energy where its real and imaginary parts determine the kink structure and width in the electron dispersion relation respectively [30, 31]. Fig. 1-8 shows the observation of the kink in the electron dispersion relation of graphene when ARPES data taken along K–M direction [26]. The electron dispersion of graphene as function wave vector changes linearly if the EPC is not considered; however, the EPC is renormalized electron dispersion and it causes the observation of the kink in electron dispersion.

It is known that the ARPES spectra around the Γ point and near the Fermi level (with binding energy around $E_b \approx 0$–3 eV) do not exist for the direct optical transition because there is no corresponding energy state [27]. However, recent ARPES experiments show that

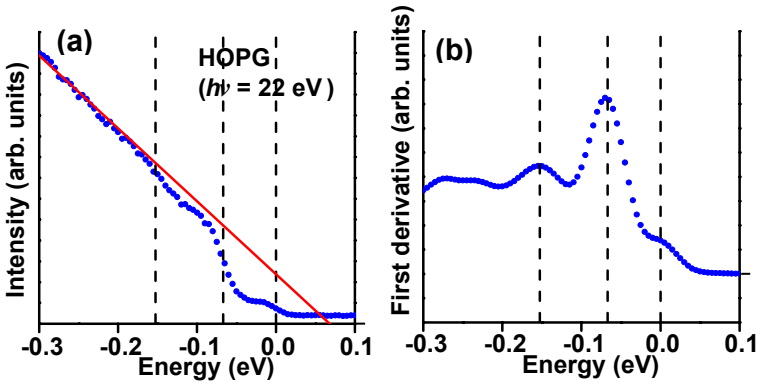

Figure 1-14: Normal-emission spectrum from HOPG showing a step-like function near 67 meV and 154 meV. (a) Integrated normal-emission spectra (b) Absolute value of the first derivative.

measurement of the ARPES intensity around the Γ point and near the Fermi level could also provide valuable information on the electron-phonon interaction [11, 12]. For example, Liu *et al.* have observed the ARPES spectra at the Γ point and near the Fermi level for graphene-based materials [11]. They pointed out that the observation of ARPES spectra originates from the *indirect transition* of electrons, which is mediated by phonons. In their experiment, the observed ARPES spectra with binding energy around 154 meV and 67 meV have been ascribed to the energy and momentum of the phonon at the K (or K$'$) point. They suggest that the electron is scattered from the K to the Γ point by emitting a phonon through the indirect transition. However, the phonon dispersion from their experiment could not be determined because they used photon energies of more than 20 eV.

Tanaka *et al.* have reported ARPES spectra of highly-oriented pyrolytic graphite (HOPG) around the Γ point and near the Fermi level for various photon energies less than 15 eV [12]. This experiment probes the energies and momenta of the electrons and phonons involved in the indirect transition, for different photon energies, so that the phonon dispersion of HOPG can be obtained (see Fig. 1-15). They found that, when the incident p-polarized photons are given to the sample surface, the ARPES intensity increases like a step-function at the binding energy around 154 meV and 67 meV for $\hbar\omega = 11.1$ eV and for $\hbar\omega = 6.3$ eV, respectively, and that the ARPES spectra cannot be observed for the $\hbar\omega = 13 - 15$ eV in their experiment (see Fig. 1-15(b)). Then, differential of the photoelectron intensity with respect to the binding energy is calculated (see Fig. 1-15(c)). Finally, Fig. 1-15(c) and (d)

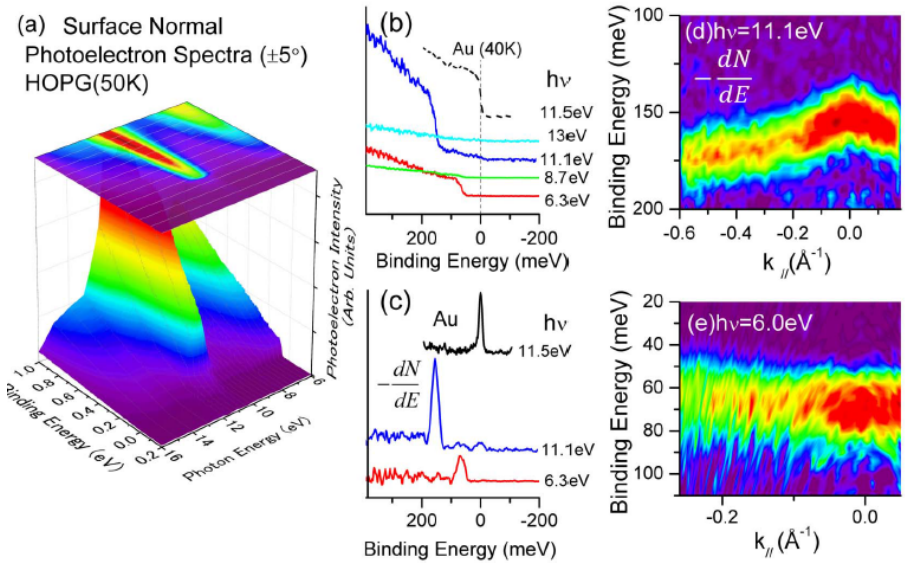

Figure 1-15: (a) Surface-normal photoelectron spectra of HOPG at 50 K taken at 6 eV $\leq$ $\hbar\omega$ $\leq$ 16 eV. (b) Typical spectra of HOPG taken at several photon energies along with that of the Au film at 40 K. (c) Differential of the photoelectron intensity with respect to the binding energy. (d,e) Differentials of the photoelectrons as a function of the parallel momentum of the electron.

Differentials of the photoelectrons as a function of the parallel momentum of the electron is plotted that it is express the phonon dispersion relation of the HOPG. However, not all the possible phonon dispersion relations of graphite could be well-resolved since HOPG is not a single crystal of graphite. Thus, the phonon modes involved in the indirect transition were not assigned properly from previous experimental measurements.

Therefore, the second subject of this thesis is studying the indirect transition of ARPES spectra near the Γ point and closed to the Fermi level. We will assign that which phonon modes can be involved in the indirect transition. Then, we will studying the photon and polarization dependent of the indirect transition ARPES spectra.

Chapter 2

Basics of graphene and graphite

Basic physical properties of graphene and graphite are reviewed in this section. The discussion includes a description of the geometrical structure, electronic properties and vibrational properties of graphene and graphite. The electronic and vibrational structures are calculated by Quantum Espresso package [32].

2.1 Geometrical structure

The electronic configuration of a free carbon atom is $1s^2 2s^2 2p^2$. When a solid is formed from carbon atoms, the electrons in the 2s and 2p orbitals form so-called hybrid orbitals that point along the chemical bonds. Depending on the crystal that we have, a different number of hybrid orbitals is required to point from two to four nearest neighbor atoms. Thus, carbon forms sp^n hybrid orbitals with $n = 2$ for graphene and graphite which are crystallized in a planar hexagonal lattice. We can define graphene as a single layer of carbon atom and it is shown in Fig. 2-1(a). Several layers of graphene sheet stacked together will form three dimensional graphite, shown in Fig. 2-1(b) and (c). The distance between planes is 0.3 nm. Bonding between layers is via weak van der Waals bonds, which allows layers of graphite to be easily separated, or to slide past each other. sp^n hybrid orbitals include two 2s electrons and one 2p electron ($2p_x$ or $2p_y$ in graphene plane) form three sp^2 hybrid orbitals and one $2p_z$ electron which is oriented perpendicular to the graphene plane. The $2p_z$ electron makes a valence π band. The π band is calculated by Wannier90 package [33] and it is shown in

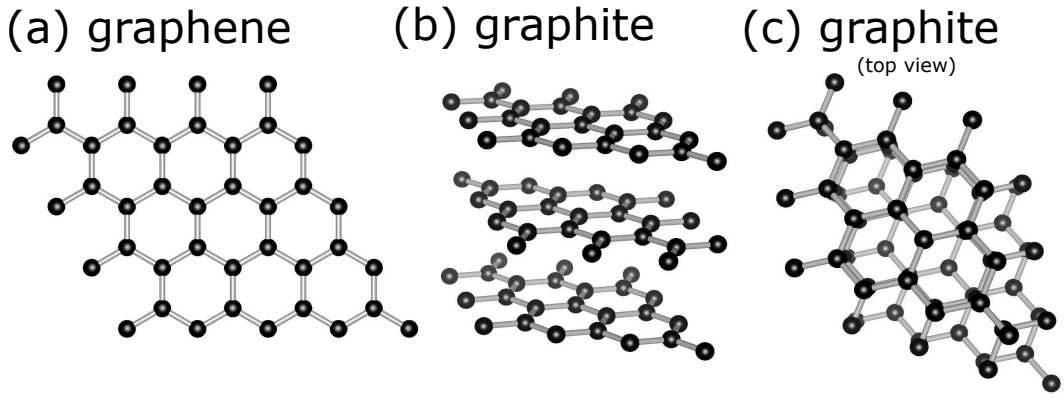

Figure 2-1: (a) Graphene is the single layer of carbon atoms hexagonal lattice. (b) Graphite has a layered, planar structure. In each layer, the carbon atoms are arranged in a hexagonal lattice. (c) Graphite (top view).

Fig. 2-2(a). The blue and red regions indicate positive and negative values of the real part of the wave function amplitudes, respectively. The in-plane sp^2 make strong σ-bonds, shown in Fig. 2-2(b) .

Figure 2-3(a) and (b) shows the unit cell and Brillouin zone of graphene, respectively. The graphene sheet is generated from the dotted rhombus unit cell shown by the lattice vector $\mathbf{a}_1$ and $\mathbf{a}_2$, which are define in (x,y) coordinate as

$$\mathbf{a}_1 = a(\frac{\sqrt{3}}{2}, \frac{1}{2}, 0), \quad \mathbf{a}_2 = a(\frac{\sqrt{3}}{2}, -\frac{1}{2}, 0), \quad \mathbf{a}_3 = c(0, 0, 1), \tag{2.1}$$

where the in-plane lattice parameter is $a = \sqrt{3}a_{CC}$ is the lattice constant for the graphene sheet and $a_{CC} = 1.42\ \mathring{A}$ is the nearest-neighbor inter-atomic distance. The out-of-plane lattice parameter for graphite is $c = 2c_0$, where $c_0 = 3.35\ \mathring{A}$, the distance between carbon atoms on the adjacent layer planes. Thus a direct lattice vector is:

$$\begin{aligned} \mathbf{R}_n &= n_1\mathbf{a}_1 + n_2\mathbf{a}_2 + n_3\mathbf{a}_3 \\ &= a\Big(\frac{\sqrt{3}}{2}(n_1 + n_2), \frac{1}{2}(-n_1 + n_2), cn_3\Big), \end{aligned} \tag{2.2}$$

where n_1, n_2 and n_3 are integers. The unit cell consists two distinct carbon atoms from the A and B sublets shown in Fig. 2-3. The reciprocal lattice vector $\mathbf{b}_1$, $\mathbf{b}_2$ and $\mathbf{b}_3$ are related

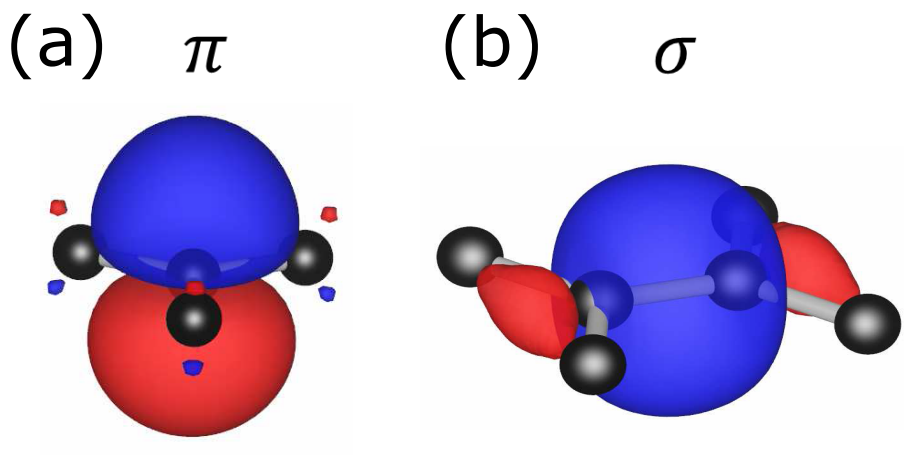

Figure 2-2: Surface plots for the maximally localized (a) π-band and (b) σ-bond orbital Wannier function. The blue and red regions indicate positive and negative values of the real part of the wave function amplitudes, respectively.

to the real lattice vectors $\mathbf{a}_1$, $\mathbf{a}_2$ and $\mathbf{a}_3$ according to the definition

$$\mathbf{a}_i \cdot \mathbf{b}_j = 2\pi\delta_{ij}, \tag{2.3}$$

where δ_{ij} is the Kronecker delta, so that $\mathbf{b}_1$ and $\mathbf{b}_2$ are given by

$$\mathbf{b}_1 = \frac{2\pi}{a}\Big(\frac{1}{\sqrt{3}}, 1, 0\Big), \quad \mathbf{b}_2 = \frac{2\pi}{a}\Big(\frac{1}{\sqrt{3}}, -1, 0\Big), \quad \mathbf{b}_3 = \frac{2\pi}{c}\Big(0, 0, 1\Big). \tag{2.4}$$

A reciprocal lattice vector is defined

$$\begin{aligned} \mathbf{G}_m &= m_1\mathbf{b}_1 + m_2\mathbf{b}_2 + m_3\mathbf{b}_3 \\ &= \Big(\frac{2\pi}{\sqrt{3}a}(m_1 + m_2), \frac{2\pi}{a}(m_1 - m_2), \frac{2\pi}{c}m_3\Big) \end{aligned} \tag{2.5}$$

The first Brillouin zone of graphene is shown as a shaded hexagon in Fig. 2-3, where Γ (center), K, K' (hexagonal corners), and M (center of edges) denote the high symmetry points.

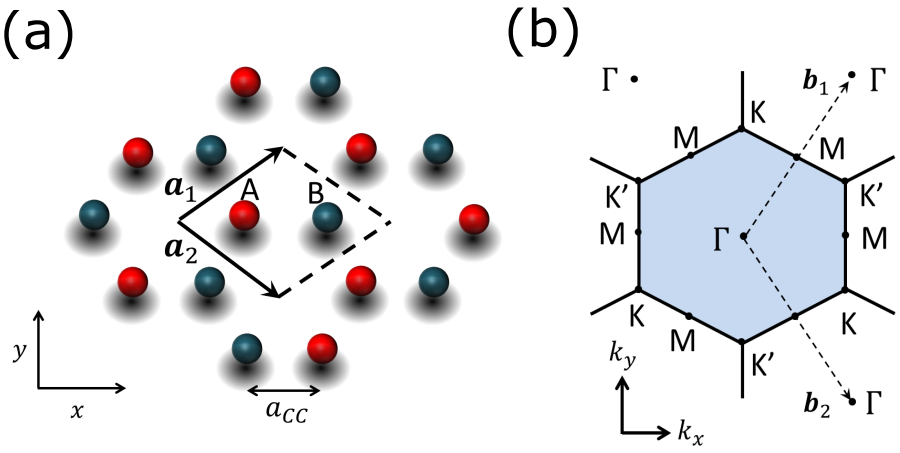

Figure 2-3: (a) The unit cell of graphene is shown as the dotted rhombus. $\mathbf{a}_1$ and $\mathbf{a}_2$ are the unit vectors of graphene. The graphene unit cell in real space contains two carbon atoms A and B. (b) Brillouin zone (BZ) of graphene is displayed as the shaded hexagon . The BZ is given by reciprocal lattice vectors $\mathbf{b}_1$ and $\mathbf{b}_2$ with $|\mathbf{b}_1| = |\mathbf{b}_2| = \frac{4\pi}{\sqrt{3}a}$. The dots labeled Γ, K, K' and M in the BZ indicate the high-symmetry points.

2.2 Electronic properties

The electron dispersion relations of graphene and graphite are calculated along Γ–K–M–Γ by the quantum Espresso (QE) package [32] and it is shown in Fig. 2-4(a) and (b). Graphene has three σ bands, formed by, s, p_x and p_y orbitals, and a π band, formed by p_z orbital. While, graphite has six σ bands, and two π and two π^*, bands because its unit cell has four atoms. Although the interlayer interaction is weak, this interaction has an effect on the π and π^* bands near the edges zone of graphite and it results in a band overlap that is responsible for the semi-metallic properties of graphite, in contrast to graphene which is a zero gap semiconductor [34]. The Brillouin zone of graphite is shown in Fig. 2-5(a). The dots labeled Γ, K, M, A, L, H in the Brillouin zone of graphite indicate the high symmetry points. Γ–A is the direction corresponding to the lattice vector normal to the surface of graphite. Fig. 2-5(b) shows the electron dispersion relation of the graphite along high symmetry points. For both graphene and graphite, we adopt the norm-conserving pseudo-potential with Perdew-Zunger (LDA) exchange-correlation scalar relativistic functional to calculate the electronic dispersion relations. The kinetic energy cut-off is taken as 60 Ry. For each atom and the kinetic energy cut-off for density potential is set 600 Ry. In order to verify the convergence of all wave functions. The k-point mesh grid for self-consistent calculation is $42 \times 42 \times 1$

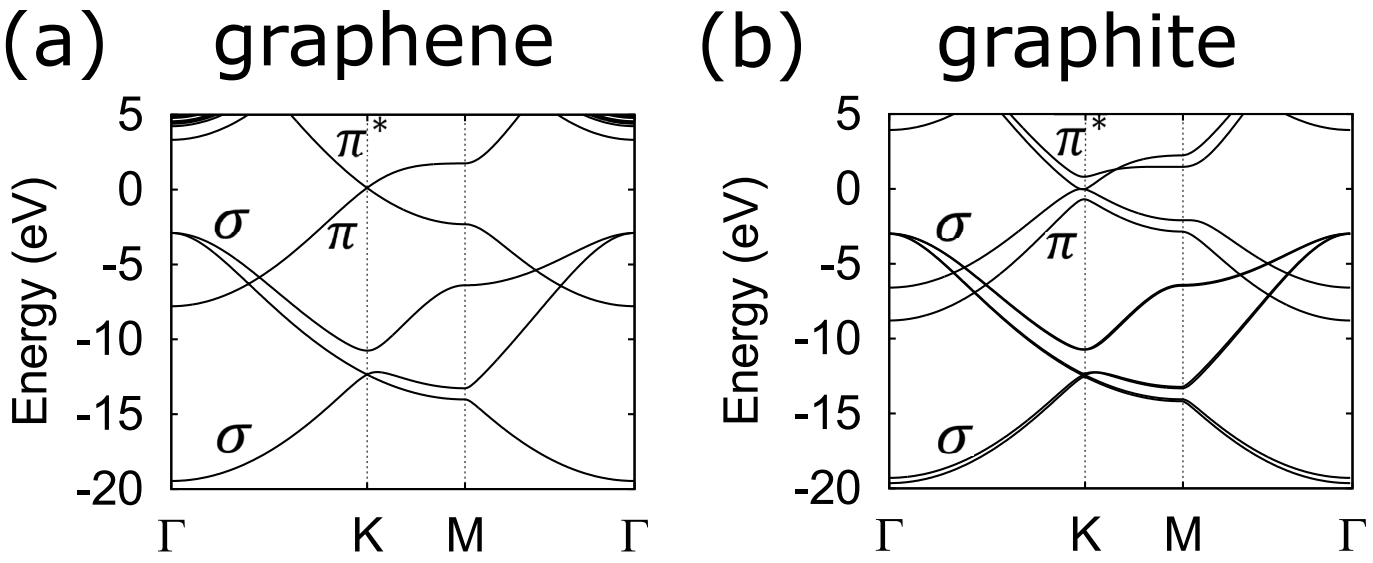

Figure 2-4: Electron energy dispersion relation in (a) graphene, (b) graphite, calculated by QE package [32] are shown along high-symmetry points Γ–K–M–Γ.

in the graphene and $20 \times 20 \times 4$ in the graphite Brillouin zones. The lattice parameter of graphene is considered $2.4\mathring{A}$ and the lattice constant for unit cell normal to graphene planes is taken as $c/a = 20.0$ and $c/a = 2.7$ for graphene and graphite, respectively.

2.3 Vibrational properties

Phonon energy dispersion relations are a fundamental physical properties of solid for determining the mechanical, thermal and other condensed matter phenomena. The phonon dispersion of graphene and graphite have been explored experimentally by inelastic neutron [35, 36], electron energy loss spectroscopy (EELS) [37, 38] and x-ray scattering [39] techniques. While, Theoretically, a number of techniques including elastic continuum model [40], force constant models [41, 42, 43], bond charge models [44] and ab-initio calculations[45, 46, 47] have been used to calculate phonon energy dispersion relations of graphene and graphite. Here, we calculate the phonon dispersion relations through QE package [32], which calculate the phonon dispersion via Density Functional Perturbation Theory (DFPT). Thus, first, we have to find the ground state atomic and electronic configuration; then, the phonon dispersion relations are calculated by DFPT (see Appendix D). To calculate the phonon energy and eigenvectors of graphene and graphite, we adopted the Perdew-Burke-Ernzerhof (PBE) generalized

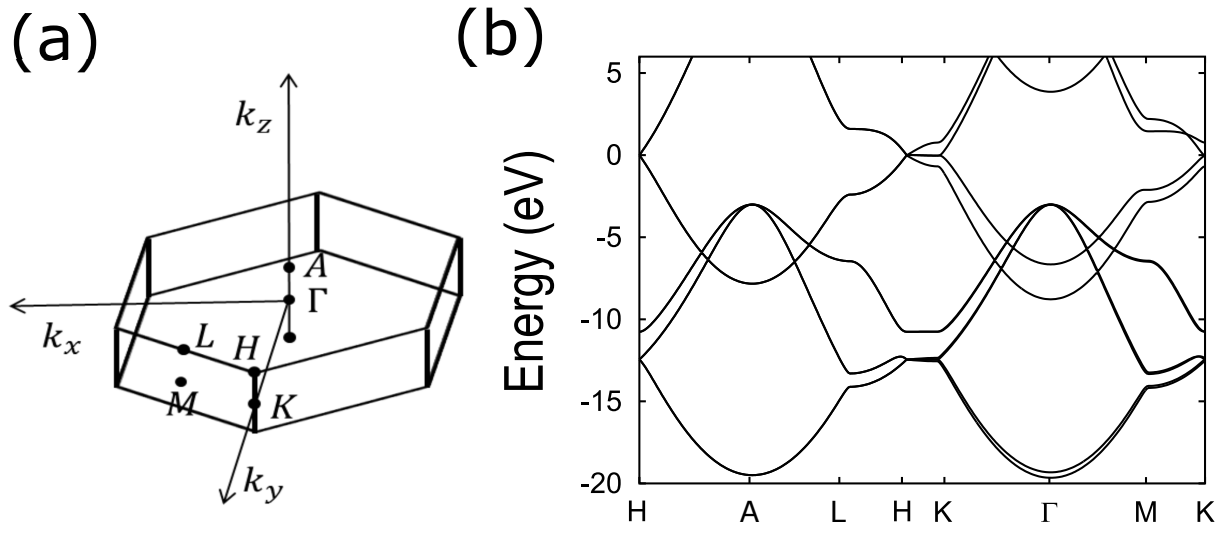

Figure 2-5: (a) Graphite Brillouin zone showing for several high symmetry points. The dots labeled Γ, K, M, A, L, H in Brillouin zone indicate the high symmetry points. (b) The electron energy dispersion relations of graphite along the high symmetry point is calculated by QE package [32].

gradient approximation (GGA) for the exchange-correlation function. The kinetic energy cut-off is taken 100 Ry for each atom and kinetic energy cut-off for density potential is set 1200 Ry. The dynamical matrix is calculated on a $6 \times 6 \times 1$ and $6 \times 6 \times 3$ q-points mesh in graphene [48].

The calculated phonon dispersion is shown in Fig. 2-6 for (a) graphene (b) graphite. Since there are four atoms in the unit cell of graphite, there will be twelve phonon modes. Most of the phonon modes are nearly doubly degenerate and similar to graphene [49, 50]. An exception is near the Γ point, where the acoustic modes of the single layer split in graphite into an acoustic mode (ZA) and an optical mode (ZO′), as shown in Fig. 2-6(a). In graphene, there are six phonon branches, four in-plane and two out-of-plane. At the Γ point, there are three acoustic (A) branches: (1) the transverse and (2) longitudinal in-plane acoustic phonon modes, which are labeled in Fig. 3 as TA and LA respectively, and (3) the out-of-plane acoustic phonon mode which is labeled ZA. Furthermore, there are three optical phonon modes: (1) the transverse and (2) longitudinal in-plane optical modes, which are labeled by TO and TA, respectively, and (3) the out-of-plane optical phonon mode, which is labeled by ZO. The phonon eigenvectors of graphene at the Γ point are also shown in Fig. 2-7 and each phonon mode is labeled. In graphite, the are twelve phonon modes because there

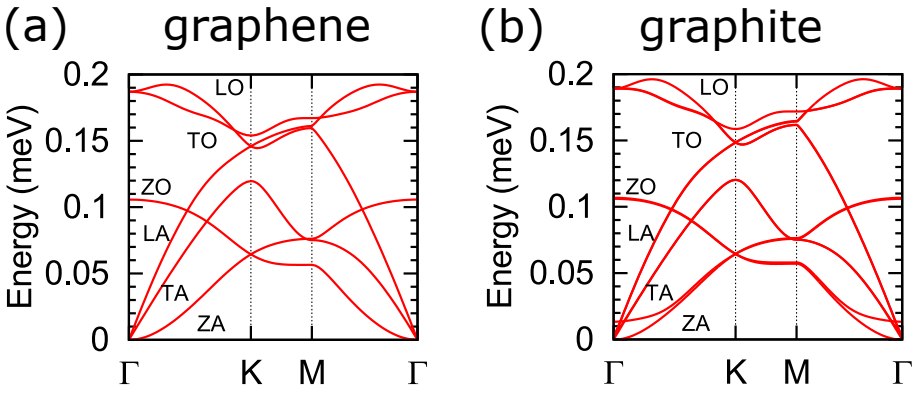

Figure 2-6: (a) Graphene phonon dispersion, (b) graphite phonon dispersion are calculated by QE along high-symmetry points Γ–K–M–Γ.

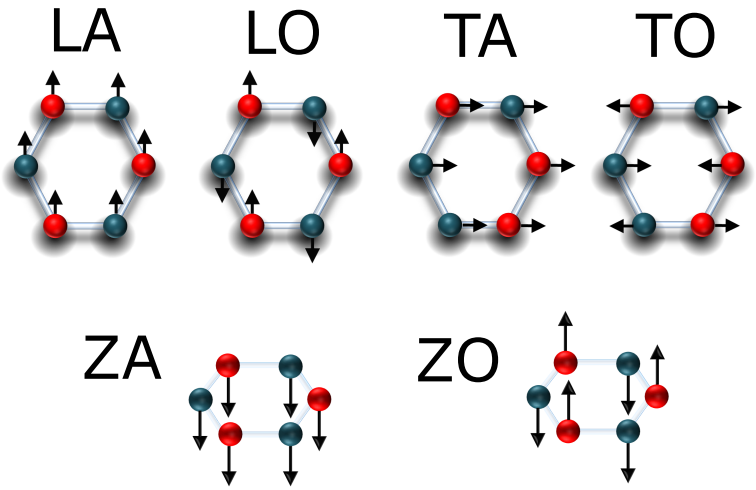

Figure 2-7: The vibration eigenvectors of graphene at the Γ point are shown and each phonon mode is labeled[51].

are four atoms in the unit cell.

Chapter 3

Direct and indirect transition of ARPES spectra

In this chapter, firstly, we will explain the experimental set-up of ARPES that we consider in this thesis. Then, the direct and indirect transitions mechanisms will be discussed. The direct transition, shown in Fig. 3-1(a), is a transition an electron from a valence band is excited to a conduction band by photoabsorption while the momentum of the electron does not change during this process. The direct transition is formulated by first-order perturbation theory. On the other hand, the indirect transition, shown in Fig. 3-1(b), is a transition that the momentum of the electron is also changed due to involving a photon, phonon or impurity interaction. The indirect process is formulated by second-order perturbation theory. In this thesis, we consider the indirect transition as a transition includes electron-photon interaction and electron-phonon coupling.

3.1 Geometry of ARPES

The experimental set-up of the direct transition is shown schematically [13], in Fig. 3-2(a). The graphene surface is irradiated by photons with the incident angle ψ with respect to z axis, normal to the surface. The emitted electrons, with emission angle θ, are analyzed with respect to their kinetic energy and momentum [22]. We can define a mirror plane which contains the incident light ($-z'$ axis), the electrons ejected from the surface, and

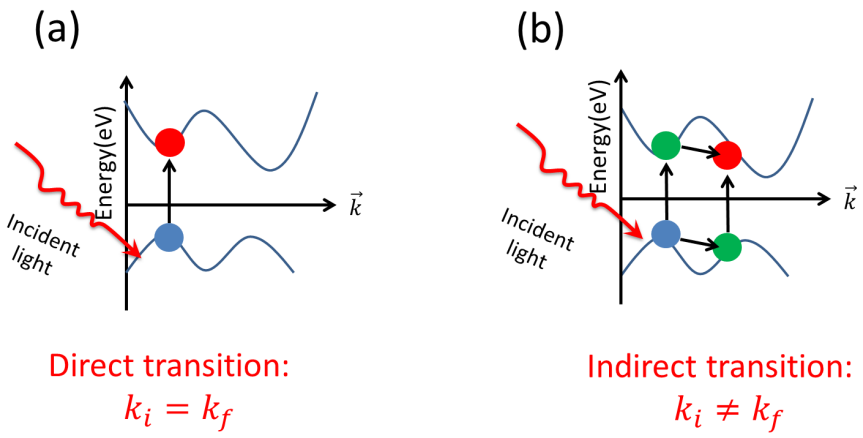

Figure 3-1: (a) The direct transition is a transition an electron from a valence band is excited to a conduction band by photoabsorption while the momentum of the electron does not change during this process. (b) the indirect transition is a transition that the momentum of the electron is also changed due to involving a photon and phonon or impurity interaction.

the axis normal to the graphene surface (z-axis). When the incident light polarization is perpendicular (parallel) to the mirror plane, the light is named s-polarized (p-polarized) light [13, 7, 8, 9]. From the z' axis viewpoint, as shown in Fig. 3-2(b), we see that the light polarization angle can be defined by angle ϕ in the $x'y'$ plane and measured by the y' axis. $\phi = 0°$ and $\phi = 90°$ corresponds to the p and s polarization, respectively.

3.2 Direct transition of ARPES

Here, we show how to calculate the electron-photon matrix elements. The Hamiltonian for a charge particle with mass m and charge $-e$ in an electromagnetic field with vector potential $\mathbf{A}^t(t)$, where t index indicates the transmitted vector potential into the solid, and a periodic crystal potential $V(\mathbf{r})$ is given by

$$H = \frac{1}{m}(-i\hbar\nabla + e\mathbf{A}^t(t))^2 + V(\mathbf{r}). \tag{3.1}$$

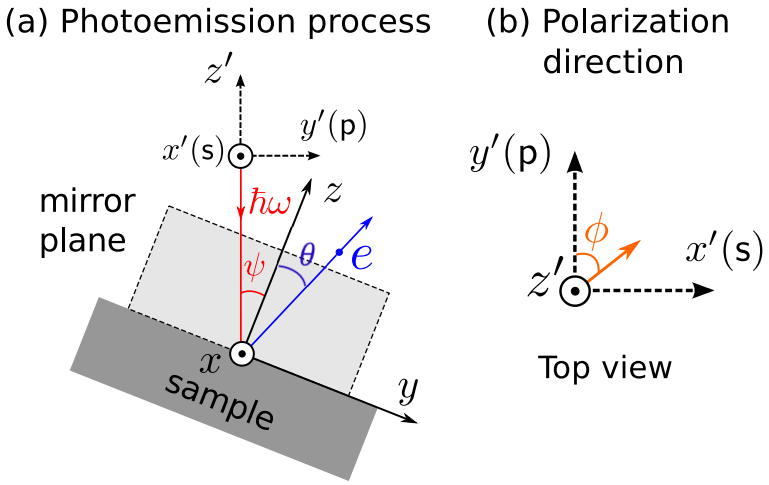

Figure 3-2: (a) Geometry of the photoemission process [13]. The incident photon with energy $\hbar\omega$ are shown by an arrow going to the graphene plane. We can define a mirror plane which contains the directions of the incident light (z' axis), the electrons ejected from the surface, and an axis (z-axis) normal to the graphene surface. The angle between incident light, the ejected electron, and the z-axis is denoted by ψ, θ. (b) Viewing the set-up from the z' axis, the light polarization angle, ϕ, is in the $x'y'$-plane and measured with respect to the y' axis. Here, $\phi = 0°$ and $\phi = 90°$ correspond to the p- and s-polarization, respectively.

If we neglect quadratic terms in $\mathbf{A}^t(t)$ as well as use the Coulomb gauge $\nabla \cdot \mathbf{A}^t(t) = 0$, the electron-photon perturbation Hamiltonian H_{opt} is given

$$H_{\text{opt}} = \frac{ie\hbar}{2m}\mathbf{A}^t(t) \cdot \nabla. \tag{3.2}$$

The vector potential in the vacuum, $A_i(t)$, can be obtained from the Maxwell equation which is given as

$$\nabla \times \mathbf{B} = \epsilon_0\mu_0\frac{\partial \mathbf{E}}{\partial t}. \tag{3.3}$$

The electric and magnetic fields of the incident light are

$$\begin{aligned} \mathbf{E}(t) &= \mathbf{E}_0 \exp(i(\mathbf{k}\cdot\mathbf{r} + i\omega t)), \\ \mathbf{B}(t) &= \mathbf{B}_0 \exp(i(\mathbf{k}\cdot\mathbf{r} + i\omega t)). \end{aligned} \tag{3.4}$$

Hence, $\mathbf{B} = \nabla \times \mathbf{A} = i\mathbf{k} \times \mathbf{A}$ and $\mathbf{B} = i\mathbf{k} \times \mathbf{B}$. We can write,

$$\nabla \times \mathbf{B} = k^2\mathbf{A} = \frac{1}{c^2}\frac{\partial \mathbf{E}}{\partial t}. \tag{3.5}$$

Since E is a plane wave we get $\frac{\partial \mathbf{E}}{\partial t} = -i\omega\mathbf{E}$ then using, $\omega = kc$, we can write $\mathbf{A}_i$ in vacuum as, $\mathbf{A}_i = -\frac{i\mathbf{E}}{\omega}$. Thus, the electrical field and vector potential direction are the same. The energy density I_0, of the electromagnetic wave is given by,

$$I_0 = \frac{EB}{\mu_0} = \frac{E^2}{\mu_0 c}. \tag{3.6}$$

The unit of I_0 is $J/m^2 sec$. Thus, the vector potential in vacuum can be written in terms of the incident light intensity, I_0 and the polarization of the electric field component $\mathbf{P}$ as,

$$\mathbf{A}_i(t) = -\frac{i}{\omega}\sqrt{\frac{I_0}{c\epsilon_0}}\exp(i\omega t)\mathbf{P} \tag{3.7}$$

where ω is the angular frequency of a photon, ε_0 is the dielectric constant of the vacuum and c is the velocity of the light.

In ARPES, we change the angle of the incident light, ψ, with respect to normal to the sample to observe different $\mathbf{k}$ points, (see Fig. 3-2(a)). The relationship between the angle of incident light and the transmitted light in the sample is given by Fresnel equation [52, 53, 54]. The Fresnel equation is obtained in the Appendix B. In Fresnel equation, for a given vector potential of incident light $\mathbf{A}_i$ in the vacuum, the vector potential of transmitted light $\mathbf{A}^t$ in the graphene with a dielectric function $\varepsilon(\omega) = \varepsilon_1(\omega) + i\varepsilon_2(\omega)$ is given as follows [52, 53, 54]:

$$\begin{aligned}
A_x^t &= \frac{2\cos\psi\sin\phi}{\cos\psi + \sqrt{\varepsilon(\omega) - \sin^2\psi}}|\mathbf{A}_i|, \\
A_y^t &= \frac{2\sqrt{\varepsilon - \sin^2\psi}\cos\psi\cos\phi}{\varepsilon(\omega)\cos\psi + \sqrt{\varepsilon(\omega) - \sin^2\psi}}|\mathbf{A}_i|, \\
A_z^t &= \frac{2\cos\psi\sin\psi\cos\phi}{\varepsilon(\omega)\cos\psi + \sqrt{\varepsilon(\omega) - \sin^2\psi}}|\mathbf{A}_i|,
\end{aligned} \tag{3.8}$$

where $A_{x,y,z}^t$ are x, y, and z component of $\mathbf{A}^t$, ϕ is the light polarization angle measured from the y' axis as shown in Fig. 3-2(b). In particular, $\phi = 0^\circ$ and $\phi = 90^\circ$ correspond to the p-polarization and s-polarization, respectively.

The electron-photon matrix element is defined by

$$M_{\text{opt}}(\mathbf{k}_i, \mathbf{k}_f) = \langle \Psi^f(\mathbf{k}_f, \mathbf{r})|H_{\text{opt}}|\Psi^i(\mathbf{k}_i, \mathbf{r})\rangle, \tag{3.9}$$

where $\Psi^i(\mathbf{k}_i, \mathbf{r})$ and $\Psi^f(\mathbf{k}_f, \mathbf{r})$ are the wave functions of an initial and a final state, respectively, and $\mathbf{k}$ is the wave vector. When we assume that vector potential is slowly changing function of $\mathbf{r}$ compared with Ψ^i or Ψ^f, the electron-photon matrix element can be written as [23]:

$$M_{\text{opt}}(\mathbf{k}_i, \mathbf{k}_f) = \mathbf{A}^t(t) \cdot \mathbf{D}(\mathbf{k}_i, \mathbf{k}_f), \tag{3.10}$$

where the dipole vector $\mathbf{D}(\mathbf{k}_i, \mathbf{k}_f)$ is defined as

$$\mathbf{D}(\mathbf{k}_i, \mathbf{k}_f) = \langle \Psi^f(\mathbf{k}_f, \mathbf{r}) | \nabla | \Psi^i(\mathbf{k}_i, \mathbf{r}) \rangle. \tag{3.11}$$

To consider the final state effects on the matrix elements, we expand the wave functions of the initial states and final states in terms of plane waves,

$$\begin{aligned} \Psi^i(\mathbf{k}_i, \mathbf{r}) &= \sum_{\mathbf{G}} C^i_{\mathbf{G}}(\mathbf{k}_i) \exp\Big(i\big(\mathbf{k}_i + \mathbf{G}\big) \cdot \mathbf{r}\Big), \\ \Psi^f(\mathbf{k}_f, \mathbf{r}) &= \sum_{\mathbf{G}} C^f_{\mathbf{G}}(\mathbf{k}_f) \exp\Big(i\big(\mathbf{k}_f + \mathbf{G}\big) \cdot \mathbf{r}\Big), \end{aligned} \tag{3.12}$$

where $\mathbf{G}$ are the reciprocal lattice vectors of graphene and $C^{i,f}_{\mathbf{G}}(\mathbf{k})$ are plane wave coefficients. We set the upper limit of photon energy as 60 eV. In this case, the optical transition occurs vertically in the $\mathbf{k}$ space, that is, $\mathbf{k}_i \approx \mathbf{k}_f = \mathbf{k}$. It should be noted that this assumption is no longer valid in the XPS measurement [55]. Inserting Eq. (A.2) to Eq. (A.1), we obtain

$$\mathbf{D}(\mathbf{k}) = i \sum_{\mathbf{G}} C^{f*}_{\mathbf{G}}(\mathbf{k}) C^i_{\mathbf{G}}(\mathbf{k}) \big(\mathbf{k} + \mathbf{G}\big). \tag{3.13}$$

ARPES intensity I as a function of wave vectors $\mathbf{k}$ and photon energy $\hbar\omega$ can be calculated by using the Fermi's golden role as follows [14]:

$$I\big(\mathbf{k}, \hbar\omega\big) \propto \sum_i \Big| \sum_f \mathbf{M}_{\text{opt}}(\mathbf{k}) \Big|^2 \delta\big(E_f - E_i - \hbar\omega\big), \tag{3.14}$$

where E_i and E_f are the energies of the initial and final states of the electron, respectively, and the delta function implies an energy conservation. The absolute value is taken after the summation of the final states to assure that all interference phenomena for a given

initial state are included [56]. In our calculations, the Dirac delta function is replaced by a Lorentzian, having a finite half-width of energy 0.6 eV which is obtained by fitting to experimental spectra. The excited electrons can escape from the surface if E_f is larger than the work function of graphene $\phi_{\rm wf} = 4.5$ eV [57].

3.3 Indirect transition AEPES

The observation of the ARPES spectra near Fermi level around Γ point can be explained by the indirect transition. Let us define the Hamiltonian H_e for electrons, H_{ph} phonon, $H_{\rm opt}$ for the electron-photon interaction and $H_{\rm epc}$ for the electron-phonon coupling. Then, the total Hamiltonian is written as

$$H = H_e + H_{ph} + H_{\rm opt} + H_{\rm epc}, \tag{3.15}$$

The unperturbed Hamiltonian of electrons and phonons is considered as $H_0 = H_e + H_{ph}$. We adopt the adiabatic approximation which implies the total wave function can be written as a product of an electron eigenstates and phonon eigenstates[31]. Thus, the eigenstates of the unperturbed Hamiltonian are expressed as

$$|j\rangle = |j\mathbf{k}\rangle, \tag{3.16}$$

where $j = i, m, f$ refers to an initial, an intermediate and a final state of the electron, respectively. $\mathbf{k}$ is an electron wave vector. The unperturbed electron and phonon dispersion relation and their eigenstates along the high symmetry points are calculated by Quantum Espresso package [32]. The calculated electron dispersions of graphene and graphite are shown in Figs. 2.4(a) and (b) and Figs. 2.5(a) and (b) , respectively.

The perturbation Hamiltonian is considered as

$$H' = H_{\rm opt} + H_{\rm epc} \tag{3.17}$$

The transition rate from an initial sate $|i\rangle$ to a final state $|f\rangle$ through a virtual state $|m\rangle$ is

given by the second-order perturbation theory [58, 59].

$$W(\mathbf{k}_f, \mathbf{k}_i) = \frac{2\pi}{\hbar}\left|S(\mathbf{k}_f, \mathbf{k}_i)\right|^2 \delta(\varepsilon_i - \varepsilon_f). \tag{3.18}$$

where ε_i and ε_f represent energy of an initial state and a final state, respectively, and $S(\mathbf{k}_f, \mathbf{k}_i)$ is

$$S(\mathbf{k}_f, \mathbf{k}_i) = \sum_m \frac{\langle f|H'|m\rangle\langle m, |H'|i\rangle}{\varepsilon_i - \varepsilon_m}. \tag{3.19}$$

Two processes can contribute to the indirect transition. These processes are depicted in Fig. 3-3(a). The first process is: (1) a photon excites an electron from the initial state $|A\mathbf{k}_i\rangle$ to a state $|B\mathbf{k}_m\rangle$, A $\rightarrow$ B. Then, the photoexcited electron from the state $|B\mathbf{k}_m\rangle$ is scattered to the final state $|D\mathbf{k}_f\rangle$ by a phonon emission, B $\rightarrow$ D. Since the sample temperature is considered at 60 K the absorption of phonon is negligible. (2) A phonon scatters an electron from the initial state $|A\mathbf{k}_i\rangle$ to a state $|C\mathbf{k}_m\rangle$, A $\rightarrow$ C. Then, a photon excites a scattered electron from the state $|C\mathbf{k}_m\rangle$ to the final state $|D\mathbf{k}_f\rangle$, C $\rightarrow$ D. These processes are expressed by the following equation:

$$\begin{aligned} S(\mathbf{k}_f, \mathbf{k}_i) = & \\ & \frac{\langle D\mathbf{k}_f, |H_{\text{epc}}|B\mathbf{k}_m\rangle\langle B\mathbf{k}_m|H_{\text{opt}}|A\mathbf{k}_i\rangle}{\varepsilon_i - \varepsilon_B} \\ & + \frac{\langle D\mathbf{k}_f|H_{\text{opt}}|C\mathbf{k}_m\rangle\langle C\mathbf{k}_m|H_{\text{epc}}|A\mathbf{k}_i\rangle}{\varepsilon_i - \varepsilon_C}, \end{aligned} \tag{3.20}$$

The energy and momentum of the processes mentioned in Eq. (3.20) are given by

$$\begin{aligned} &\mathbf{k}_f = \mathbf{k}_i + \mathbf{q} \\ &\varepsilon_i - \varepsilon_f = E_i(\mathbf{k}_i) + \hbar\omega - \hbar\omega_q^\alpha - E_f(\mathbf{k}_f) \\ &\varepsilon_i - \varepsilon_B = E_i(\mathbf{k}_i) + \hbar\omega - E_B(\mathbf{k}_i) \\ &\varepsilon_i - \varepsilon_C = E_i(\mathbf{k}_i) - \hbar\omega_q^\alpha - E_C(\mathbf{k}_f). \end{aligned} \tag{3.21}$$

where $\hbar\omega$ denotes the photon energy and $\hbar\omega_q^\alpha-$ refers to the energy of α-nth phonon branch

with the wave vector $\mathbf{q}$. We note since the applied photon energy is less than $\hbar\omega = 15$ eV in this study, the optical transition occurs vertically [55].

In order to relate the measured energy distribution curve (EDC), namely $I(E, \hbar\omega)$ to the theoretical photoemission, one has to integrate over all initial states and final states. The summation on initial states and final states can perform independently when the experimental conditions are chosen [14]; hence, we have

$$\begin{aligned} I(E, \hbar\omega) \propto & \\ & \sum_{i,f} \int d\mathbf{k}_i d\mathbf{k}_f M(\mathbf{k}_f, \mathbf{k}_i) \times \\ & \delta(\varepsilon_i - \varepsilon_f)\delta(E - \varepsilon_f + \phi_{wf})(N_q^\alpha + 1) f_F^{occ}, \end{aligned} \tag{3.22}$$

where $\phi_{wf} = 4.5$ eV is the graphene work function [57], f_F^{occ} denotes Fermi-Dirac distribution function of an occupied state and N_q^α is the phonon quantum number of mode α with wave vector $\mathbf{q}$. The second delta function ensures that the photoelectrons have a higher energy than the graphene work function. Therefore, in order to determine the indirect ARPES intensity, we need to calculate the electron-phonon coupling and electron-photon interaction matrix elements.

3.3.1 Electron-phonon coupling

Let us define the equilibrium position of an atom $\sigma = A, B$ in the nth unit cell by $\mathbf{R}_\sigma^n$

$$\mathbf{R}_\sigma^n = \mathbf{R}_n + d_\sigma \tag{3.23}$$

and displacement vector of the atom by $S_{n,\sigma}^\alpha(t)$ and $\alpha = 1, \ldots, 6$ denotes the phonon modes.

The changes of the potential energy due to the lattice displacement is given by

$$\begin{aligned} H_{epc} &= \sum_{n,\sigma} [V_n(\mathbf{r} - \mathbf{R}_\sigma^n + S_{n,\sigma}^\alpha(t)) - V_n(\mathbf{r} - \mathbf{R}_\sigma^n)] \\ &= \sum_{n,\sigma} S_{n,\sigma}^\alpha(t) \cdot \nabla_{\mathbf{R}_\sigma^n} V_n(\mathbf{r} - \mathbf{R}_\sigma^n). \end{aligned} \tag{3.24}$$

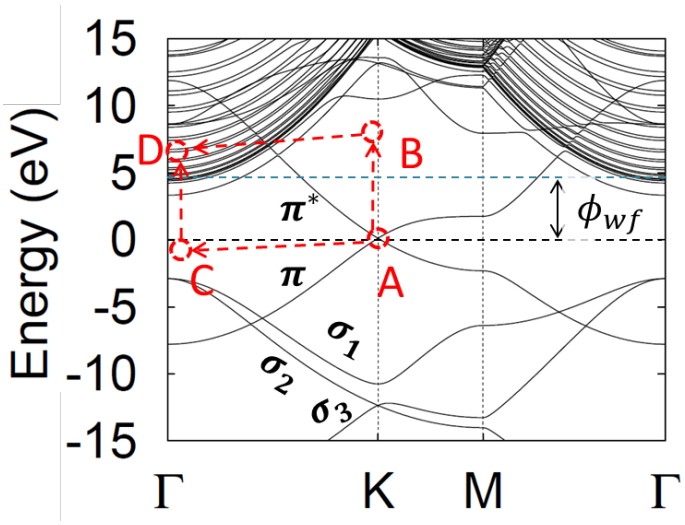

Figure 3-3: The electronic energy dispersion relation of graphene (b) are calculated by first-principles calculation is plotted along the high symmetry points Γ–K–M–Γ up to 15 eV. (1)$A \rightarrow B \rightarrow D$, a photon excites an electron from the initial state $|A\mathbf{k}_i\rangle$ to a virtual state $|B\mathbf{k}_i\rangle$, $A \rightarrow B$. Then, a phonon scatters the electron from the virtual state $|B\mathbf{k}_i\rangle$ to the final state $|D\mathbf{k}_f\rangle$, $B \rightarrow D$. (2) $A \rightarrow C \rightarrow D$, a phonon scatters an electron from the initial state $|A\mathbf{k}_i\rangle$ to a virtual state $|C\mathbf{k}_f\rangle$, $A \rightarrow C$. Then, a photon excites an electron from the virtual state $|C\mathbf{k}_m\rangle$ to the final state $|D\mathbf{k}_f\rangle$, C $\rightarrow$ D.

The lattice displacement vector $S^{\alpha}_{n,\sigma}(t)$ is given by

$$S^{\alpha}_{n,\sigma}(t) = A^{\alpha}_{\rho}(\mathbf{q}) e^{\alpha}_{\sigma}(\mathbf{q}) e^{i\mathbf{q}\cdot\mathbf{R}^n} e^{\pm i\omega^{\alpha}(\mathbf{q})t} \tag{3.25}$$

where A^{α}_{ρ} is atomic vibration amplitude. The $\pm$ and ρ indices refer to whether a phonon is emitted (" $-$ " and $\rho = E$) or absorbed (" $+$ " and $\rho = A$). $e^{\alpha}(\mathbf{q})$ is the unit vector of the lattice displacement vector. $\omega(\mathbf{q})$ is the angular frequency of phonon with a wave vector $\mathbf{q}$. The amplitude of the vibration, A^{α}_{ρ}, is given by

$$A^{\alpha}_{\rho}(\mathbf{q}) = \sqrt{\frac{2\hbar N^{\alpha}_{\rho}(\mathbf{q})}{m\omega^{\alpha}(\mathbf{q})N}} \tag{3.26}$$

the number of phonons in the vibrational mode with index α given by N^{α}_{ρ} and the number of atoms N that contribute to the phonon. $m = 1.9927 \times 10^{-26}$ Kg is the mass of a carbon atom.

$$N^{\alpha}_{A}(q) = \frac{1}{\exp(\frac{\hbar\omega^{\alpha}(\mathbf{q})}{k_B T}) - 1} \qquad N^{\alpha}_{E}(q) = N^{\alpha}_{A}(q) + 1 \tag{3.27}$$

We follow the rigid-ion approximation where the potential V follows rigidly the motion of the ions [31, 60]. Thus, the EPC Hamiltonian can be expressed by

$$H_{epc} = -\sum_{n=0}^{N-1}\sum_{\sigma=A,B}\sum_{\alpha=1}^{6} A_{\rho}^{\alpha}(\mathbf{q}) S_{n,\sigma}^{\alpha}(t)\cdot\nabla_{\mathbf{r}} V_n(\mathbf{r}-\mathbf{R}_{\sigma}^{n,\alpha}). \tag{3.28}$$

Using the perturbation theory, the non-zero matrix elements for this potential is given by

$$M_{epc}^{v,v'}(\mathbf{k}_f,\mathbf{k}_i) = \langle \mathbf{k_f}|H_{epc}|\mathbf{k_i}\rangle, \tag{3.29}$$

where v and v' indicate different electron bands energies. To calculate the electron-phonon matrix elements for different bands, we expand the wave function of the initial states and final states in terms of plane waves,

$$\begin{aligned} |\mathbf{k}_i^{v}\rangle &= \frac{1}{\sqrt{V}}\sum_{\mathbf{G}} C_{\mathbf{G}}^{i,v}(\mathbf{k}_i)\exp\Big(i\big(\mathbf{k}_i+\mathbf{G}\big)\cdot\mathbf{r}\Big), \\ |\mathbf{k}_f^{v'}\rangle &= \frac{1}{\sqrt{V}}\sum_{\mathbf{G}'} C_{\mathbf{G}'}^{f,v'}(\mathbf{k}_f)\exp\Big(i\big(\mathbf{k}_f+\mathbf{G}'\big)\cdot\mathbf{r}\Big), \end{aligned} \tag{3.30}$$

where V is the volume of the sample, $\mathbf{G}$ represents the reciprocal lattice of graphene and $C_{\mathbf{G}}^{i,f,v,v'}$ is the plane-wave coefficients. Thus, the electron-phonon matrix elements is given by

$$\begin{aligned} M_{epc}^{v,v'}(\mathbf{k}_f,\mathbf{k}_i) = \frac{1}{V}\sum_{n=0}^{N-1}\sum_{\alpha=1}^{6}\sum_{\sigma=A,B}\sum_{\mathbf{G},\mathbf{G}'} C_{\mathbf{G}'}^{*f,v'}(\mathbf{k}_f) C_{\mathbf{G}}^{i,v}(\mathbf{k}_i) \\ \times A_{\rho}^{\alpha}(\mathbf{q}) e^{i\mathbf{q}\cdot\mathbf{R}^n} e_{\sigma}^{\alpha}(\mathbf{q})\cdot\mathbf{m}_D(\mathbf{k_f},\mathbf{k_i}), \end{aligned} \tag{3.31}$$

where $\mathbf{m}_D$ is expressed by

$$\mathbf{m}_D(\mathbf{k}_f,\mathbf{k}_i) = \int e^{i(\mathbf{k}_f-\mathbf{k}_i+\mathbf{G}'-\mathbf{G})\cdot\mathbf{r}}\nabla_{\mathbf{r}} V(\mathbf{r}-\mathbf{R}_{\sigma}^{n})d\mathbf{r}. \tag{3.32}$$

We multiply the Eq. (3.31) by

$$1 = e^{i(\mathbf{k}_f-\mathbf{k}_i+\mathbf{G}'-\mathbf{G})\cdot\mathbf{R}_{\sigma}^{n}} e^{-i(\mathbf{k}_f+\mathbf{G}')\cdot\mathbf{R}_{\sigma}^{n}} e^{i(\mathbf{k}_i+\mathbf{G})\cdot\mathbf{R}_{\sigma}^{n}}, \tag{3.33}$$

thus, the electron-phonon matrix elements by changing variables $\mathbf{r}' = \mathbf{r} - \mathbf{R}_\sigma^n$ and $d\mathbf{r}' = d\mathbf{r}$ is given by

$$\begin{aligned} M_{epc}^{v,v'}(\mathbf{k}_f, \mathbf{k}_i) = \frac{1}{V} \sum_{n=0}^{N-1} \sum_{\alpha=1}^{6} \sum_{\sigma=A,B} \sum_{\mathbf{G},\mathbf{G}'} C_{\mathbf{G}'}^{*f,v'}(\mathbf{k}_f) C_{\mathbf{G}}^{i,v}(\mathbf{k}_i) \\ \times A_\rho^\alpha(\mathbf{q}) e^{-i(\mathbf{k}_f - \mathbf{k}_i + \mathbf{G}' - \mathbf{G})\cdot \mathbf{R}_\sigma^n} e^{i\mathbf{q}\cdot\mathbf{R}^n} e_\sigma^\alpha(\mathbf{q}) \cdot \mathbf{m}_D(\mathbf{k}_f, \mathbf{k}_i), \end{aligned} \tag{3.34}$$

and the $\mathbf{m}_D(\mathbf{k}_f, \mathbf{k}_i)$ is expressed by

$$\mathbf{m}_D(\mathbf{k}_f, \mathbf{k}_i) = \int e^{i(\mathbf{k}_f - \mathbf{k}_i + \mathbf{G}' - \mathbf{G})\cdot\mathbf{r}'} \nabla_{\mathbf{r}'} V(\mathbf{r}') d\mathbf{r}'. \tag{3.35}$$

Now, the momentum conservation rule can be obtained by replacing Eq. (3.23) into Eq. (3.34) and sum over the lattice vector $\mathbf{R}^n$, and using lattice point and reciprocal lattice properties that $e^{iG\cdot R^n} = 1$

$$\sum_{n=0}^{N-1} e^{-i(\mathbf{k}_f - \mathbf{k}_i - \mathbf{q} + \mathbf{G}' - \mathbf{G})\cdot\mathbf{R}^n} = \delta_{\mathbf{k}_f, \mathbf{k}_i + \mathbf{q}}. \tag{3.36}$$

Thus, the electron-phonon matrix elements become

$$\begin{aligned} M_{epc}^{v,v'}(\mathbf{k}_f, \mathbf{k}_i) = \frac{1}{V} \sum_{\alpha=1}^{6} \sum_{\sigma=A,B} \sum_{\mathbf{G},\mathbf{G}'} C_{\mathbf{G}'}^{*f,v'}(\mathbf{k}_f) C_{\mathbf{G}}^{i,v}(\mathbf{k}_i) \\ \times A_\rho^\alpha(\mathbf{q}) e^{-i(\mathbf{k}_f - \mathbf{k}_i + \mathbf{G}' - \mathbf{G})\cdot \mathbf{d}_\sigma} \delta_{\mathbf{k}_f, \mathbf{k}_i + \mathbf{q}} e_\sigma^\alpha(\mathbf{q}) \cdot \mathbf{m}_D(\mathbf{k}_f, \mathbf{k}_i). \end{aligned} \tag{3.37}$$

In order to proceed the calculation, we expand the ion potential of a free carbon atom, obtained by ab-initio method [61, 62, 63], into a Gaussian basis function. In the expansion of the ion potential $V(\mathbf{r})$, screening from the two 1s core electrons is considered and then the fitted potential has the spherical symmetry. Since $V(r)$ goes to minus infinity for $r \to 0$, it is not possible to fit the potential directly. Instead we fit $rV(r)$ and divide later by r. The potential is given by

$$V(\mathbf{r}) = -\frac{1}{r} \sum_{p=1}^{4} v_p \exp\left(\frac{-\mathbf{r}^2}{2\tau_p^2}\right). \tag{3.38}$$

Table 3.1: The coefficient for the potential is given by substituting v_p and τ_p into Eq. (3.38)[61, 62, 63]. The unit of v_p is [Hartree $\times$ at.u.] and τ_p is given [at.u.] (1 Hartree is 27.211 eV, 1 a.u. is 0.529177) Angstrom.

p	1	2	3	4
v_p	-2.13	-1.00	-2.00	-0.74
τ_p	0.25	0.04	1.00	2.80

The fitting parameters for the potential in Eq. (3.38) is listed in table I.

Thus, by putting Eq. (3.38) into the Eq. (C.3), and considering momentum conservation $\mathbf{m}_D(\mathbf{k_f}, \mathbf{k_i})$ becomes

$$\mathbf{m}_D(\mathbf{k_f}, \mathbf{k_i}) = -\, i2\pi\sqrt{2\pi}\frac{\mathbf{Q}}{|\mathbf{Q}|} \times \sum_{p=1}^{4} v_p\tau_p \mathrm{Erfi}(\frac{(|\mathbf{Q}|)\tau_p}{\sqrt{2}})\times \exp\,(-(\frac{(|\mathbf{Q}|)\tau_p}{\sqrt{2}})^2) \tag{3.39}$$

where $\mathbf{Q} = \mathbf{q} + \mathbf{G}' - \mathbf{G}$ and $\mathrm{Erfi}(z)$ is the imaginary error function.

Furthermore, the summation on the atomic position $\sigma = A, B$ for the LO and TO branches zone center phonon $\mathbf{q} = 0$ can be done analytically. Thus, when $\mathbf{k}_i = \mathbf{k}_f = \mathbf{k}$ along the chosen energy counter the absolute value of the electron phonon coupling matrix elements $|M(\mathbf{k})|$ are proportional to $|\sin\theta|$ and $|\cos\theta|$ for LO and TO modes, respectively, where $\tan\theta = k_y/k_x$ [61].

In order to approximate the m_D in two limits for long and show wave vector, we expand $\exp\,(-z^2)$, and $\mathrm{Erfi}(z)$ as follow

$$\exp\,(-z^2) = 1 - z^2 + \frac{1}{2}z^4 - \frac{1}{6}z^6 + \frac{1}{24}z^8 + ... \tag{3.40}$$

It has series $z \to 0$ given by

$$\mathrm{Erfi}(z) = \pi^{-1/2}(2z + \frac{2}{3}z^3 + \frac{1}{5}z^{+}\frac{1}{21}z^z + ...). \tag{3.41}$$

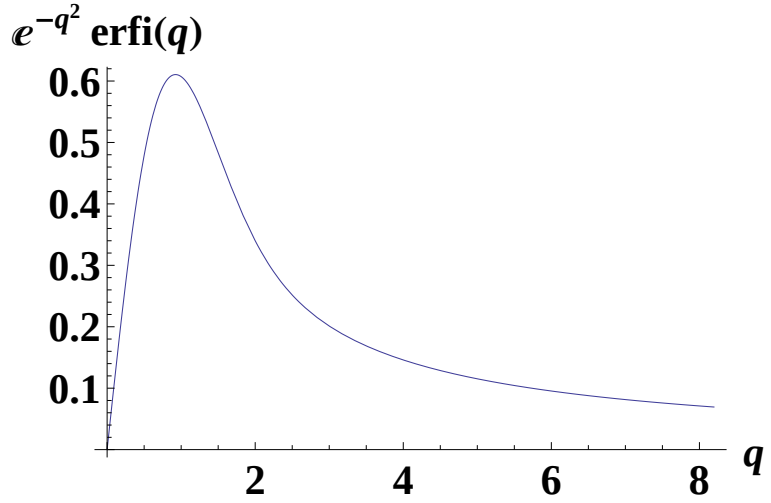

Figure 3-4: To approximate the EPC coupling for the short and long wave phonons, we expand $\text{Erfi}(q) \times \exp(-q^2)$.

when $z \to \infty$ we have

$$\text{Erfi}(z) = -i + \frac{e^{z^2}}{\sqrt{\pi}}(z^{-1} + \frac{1}{2}z^{-3} + \frac{3}{4}z^{-5} + \frac{15}{8}z^{-7} + ...). \tag{3.42}$$

We plot the following function, $\text{Erfi}(q) \times \exp(-q^2)$, in Fig. 3-4, to approximate when the EPC for the short and long wave phonon, $q \to 0$ and $q \to \infty$ respectively. Then, we can approximate the EPC for the $q \to 0$ and $q \to \infty$. In the case of short wave, if we assume $\omega_{LA}(\mathbf{q}) = C_{LA}q$ for LA phonon mode and expand $\mathbf{m}'_D(\mathbf{k_f}, \mathbf{k_i})$ for the $\mathbf{q} \to 0$, the expanded EPC can be approximated by $\mathbf{q}^{1/2}$ [62]. In the case of short wave and optical phonon modes, we can assume that the phonon frequency is almost constant $\omega(\mathbf{q}) \approx const$; the expanded EPC is proportional to $\mathbf{q}^{-1}$ and finally becomes constant [64].

Chapter 4

Symmetry selection rules of ARPES

In this Chapter, we will study the selection rules in the ARPES for the direct and indirect transitions. We will introduce C_{2v} symmetry briefly because the the experimental measurements and theoretical calculation presented in this thesis is along Γ–K-M which have C_{2v} symmetry. Then, the selection rules for the direct and indirect transition will be obtained. Studying the selection rules in the APRES is enable us to understand when transitions is allowed and there is non-negligible ARPES spectra.

4.1 Graphene and graphite symmetry

The classification of objects according to symmetry elements corresponding to operations that leave at least one common point unchanged give rise to the point group. In graphene and graphite, the three high-symmetry points Γ, K(or K'), and M correspond to the D_{6h}, D_{3h} and D_{2h} point group symmetries, respectively. The electronic states and vibrational modes along the K'–Γ–K and K'–M–K lines, shown in Fig. 4-1(a) with red dots line, belong to the C_{2v} point group, while any other general $\mathbf{k}$ points belong to the C_{1h} point group [65, 66, 67]. The C_{2v} point group has three kinds of symmetry operations. (1) The identity E, consists of doing nothing: the corresponding symmetry element is an entire object. In general, object undergo this symmetry operation. (2) The 2-fold rotation about an 2-fold axis of symmetry, C_2 is a rotation through the angle 180°. (3) The reflection in a mirror plane, σ_v where v denotes the vertical. In Fig. 4-1(b), the stereographic projections of the $C_{2v}(mm2)$ is shown.

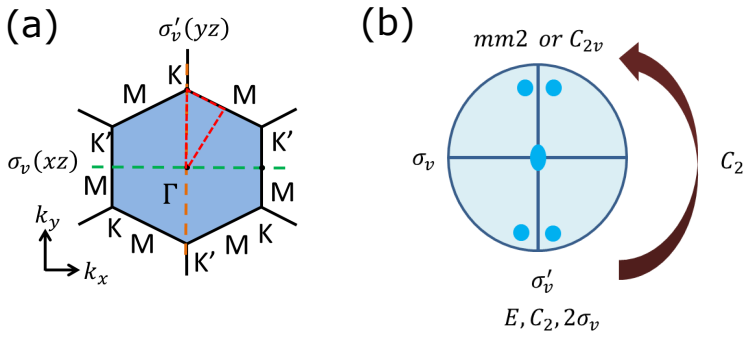

Figure 4-1: (a) Graphene and graphite have C_{2v} group symmetry along the high symmetry points: Γ–K–M–Γ. C_{2v} symmetry has 4 symmetry operations, E, C_2, $\sigma_v(xz)$ and $\sigma_v'(yz)$. The two mirror plane symmetry are shown in the BZ of graphene. (b) The stereographic projections of the $C_{2v}(mm2)$ is shown. It is seen that how the symmetry operations keep the C_{2v} symmetry.

Table 4.1: Character table of the $C_{2v}(2mm)$ point group.

	E	C_2	$\sigma_v(xz)$	$\sigma_v'(yz)$	bases
A_1	1	1	1	1	z, ∇_z
A_2	1	1	-1	-1	R_z
B_1	1	-1	1	-1	x, R_y, ∇_x
B_2	1	-1	-1	1	y, R_x, ∇_y

It is seen how the E, C_2 and σ_v operations do not change the figure. The C_{2v} group has four irreducible representations $\{A_1, A_2, B_1, B_2\}$ as shown in Table I. A is used if the character under the principle rotation is $+1$, while B is used if the character is -1.

4.2 Direct transition symmetry selection rules

In Figs. 4-2(a)-(c), we show the experimental ARPES spectra near the Dirac point for several polarization angles in which the photon energy is fixed at $\hbar\omega = 50$ eV and the incident angle is $\psi = 18°$. The polarization angles $\phi = 0°$ and $\phi = 90°$ in Figs. 4-2(a) and 4-2(c) correspond to the case of pure p- and s-polarized light, respectively, while $\phi = 78°$ in Fig. 4-2(b) has some contributions from both the p- and s-polarized light. The π and π^* bands of graphene along the Γ–K direction near the Dirac point are brightened by the p- and s-polarized light (in the case of n-doped graphene), as shown in Figs. 4-2 (a) and 4-2(c), respectively. On the other hand, for the direction along K–M, the π and π^* bands are brightened by the s- and p-polarized light, respectively. The energy band brightened by the p-polarized light

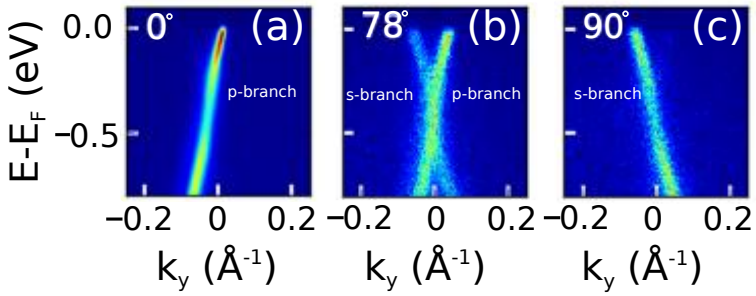

Figure 4-2: ARPES spectra of graphene near the Dirac point (K) as a function of the wave vector for: (a) the p-polarized light at $\phi = 0°$, (b) the $\phi = 78°$ polarized light, and (c) the s-polarized light at $\phi = 90°$. The photon energy is $\hbar\omega = 50$ eV and the incident angle is $\psi = 18°$. In this case, $k_y = 0$ refers to the K point and $k_y > 0 (k_y < 0)$ is along K–M (K–Γ) direction.

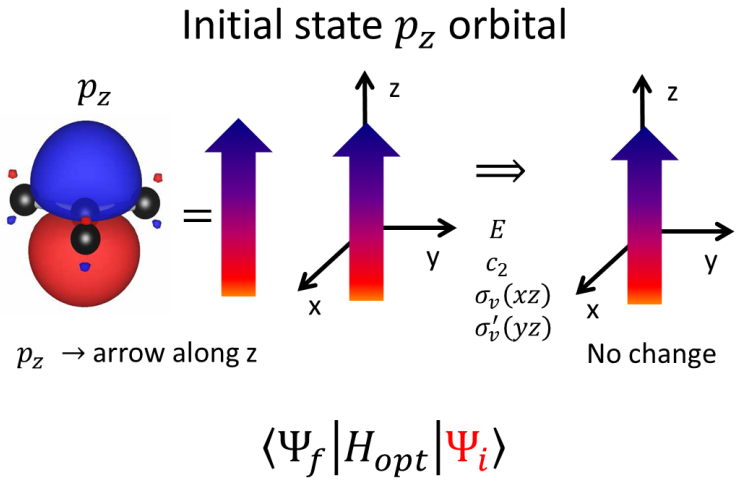

Figure 4-3: p_z orbital as an initial state has C_{2v} symmetry. p_z orbital can be considered as an arrow along the z axis that the E, C_2 and $2\sigma_v$ symmetry operations do not change its symmetry.

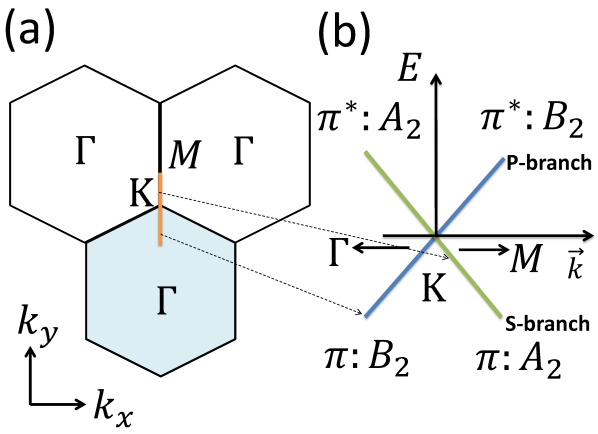

Figure 4-4: (a) Hexagonal Brillouin zone of graphene (shaded area). The ARPES calculation is performed near the K point along the line Γ–K and K–M, which is shown by the orange line. (b) The schematic linear band structure of graphene along Γ–K and K–M on the orange color line with their representation of point group symmetry. The p-polarized light illuminates the blue energy band with B_2 symmetry and the s-polarized light illuminates the green energy band with A_2 symmetry.

is referred to as the p-branch, while that brightened by the s-polarized light is called the s-branch. In the case of other polarization angles which are not equal to $\phi = 0°$ and $\phi = 90°$, we might expect some brightening on either the p-branch or the s-branch, such as the one shown in Fig. 4-2(b). In order to explain the polarization dependence of the π and π^* bands near Dirac point, the symmetry of the wave function and electron-photon matrix element can be analyzed by the group theory [68, 22].

The optical dipole selection rule imposes non-zero matrix element for the transition which satisfies

$$\Gamma_o \subset \Gamma_f \otimes \Gamma_i \tag{4.1}$$

where Γ_i, Γ_f and Γ_o are, respectively, irreducible representations for the initial state, the final state of electron wave function, and x, y, z component of ∇ in Eq. 4.1. In the case of graphene, the point group symmetry of wave functions along the Γ–K and K–M lines in Fig. 4-4(a) belongs to C_{2v} point group [65, 66, 67]. Studying the symmetry of wave functions from first principles calculation also indicates that there is a C_{2v} symmetry along the high symmetry points of graphene near the Dirac point. The π and π^* bands, as initial states, in graphene make from p_z orbital. p_z orbital has C_{2v} point group symmetry. In Fig. 4-2, we

Table 4.2: Product of C_{2v} representation, $\Gamma_f \otimes \Gamma_i$, with the initial states $\Gamma_i = \{A_2, B_2\}$ and the final states $\Gamma_f = \{A_1, B_2\}$. The s-polarized light is parallel to x axis and it has B_1 symmetry, while the p-polarized light is coplanar with the mirror plane and it has both y and z component of the light which transform as A_1 and B_2 symmetry.

$\downarrow E_f/E_i \rightarrow$	A_2	B_2
A_1	A_2	$B_2(p)$
B_2	$B_1(s)$	$A_1(p)$

show that p_z orbital. p_z orbital can be considered as an arrow along the z axis that the E, C_2 and $2\sigma_v$ symmetry operations do not change its symmetry. The calculation shows that π and π^* bands of graphene along the Γ–K (K–M) line have B_2 (A_2)and A_2 (B_2) symmetry, respectively. We give a schematic illustration for the symmetry of the wave function for each band in Fig. 4-4(b).

In ARPES, to have a non-zero intensity in detector, the integral of the $\langle \Psi^f | \mathbf{A} \cdot \mathbf{P} | \Psi^i \rangle$ must be an even function under reflection with respect to the mirror plane $\sigma_v'(yz)$ which was defined in Fig. 3.1. Moreover, the final state the photoemitted electron which is observable in the detector must be an even function under reflection with respect to the mirror plane $\sigma_v'(yz)$ [22, 6, 69, 8]. Hence, the final state can have either $\Gamma_f = A_1$ or B_2 symmetry. As a result, applying the p-polarized light which has even symmetry with respect to $\sigma_v'(yz)$ brightens the π band along Γ–K line and π^* band along K–M line with same B_2 symmetry, comparably the dipole vector in the direction of y- and z-axes. On the other hand, the s-polarized light which has odd symmetry with respect to $\sigma_v'(yz)$ brightens π band along $K - M$ and π^* band along Γ–K, corresponding to the dipole vector in the direction of x-axis [22, 7]. Consequently, it can be the origin of the chiral dependence of the graphene bands near the Dirac point based on the calculation of the dipole vector. Therefore, applying p- or s-polarized light imposes a specific optical transition selection rule for the direction of ejected electron which is summarized in Table II. It is noted that in the product table (Table II), the A_2 symmetry does not refer any dipole vector direction.

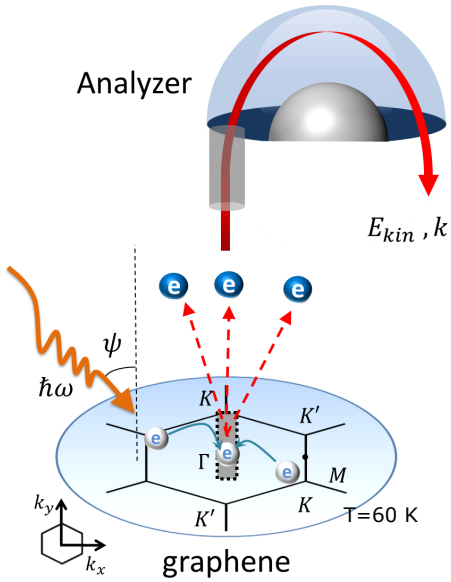

Figure 4-5: The indirect scattering of electron. An electron around the K or K' point scatters around the Γ point by the indirect transition. The shaded region line along Γ–K what we observed E_{kin} and $\mathbf{k}$.

4.3 Indirect transition

The geometry of the indirect scattering of electrons is schematically illustrated in Fig.4 4-5. The electrons around the K or K′ point can scatter to the region near the Γ point by an indirect transition. The shaded region along Γ–K direction displays the location where the photoemission electrons are measured in the ARPES experiment. The scattering processes are limited by the selection rules arisen from the presence of symmetries that are enforced by conservation laws. There are three kinds of the symmetry selection rules involved in the indirect transition that restrict the observation of a certain phonon branch: a) The lattice symmetry [11]. b) Optical and lattice vibration transition selection rules [68]. c) Conservation of parity under reflection [22]. Therefore, to understand the indirect transition mechanism we will discuss the mentioned selection rules.

a) The lattice symmetry: We consider electrons are scattered by phonons from around the K or K' points into a certain $\mathbf{k}$ as shown by a yellow circle at the Γ–K line in Fig. 4-6 (a). The phonon wave vectors which scatter electrons from the K and K' into $\mathbf{k}$, are shown by the red solid and green dot arrows, respectively. The phonon wave vectors $\mathbf{q}_1, \mathbf{q}_3, \mathbf{q}_5$ and $\mathbf{q}_2, \mathbf{q}_4, \mathbf{q}_6$ indicate scattering from the K and K' points, respectively. However, only two

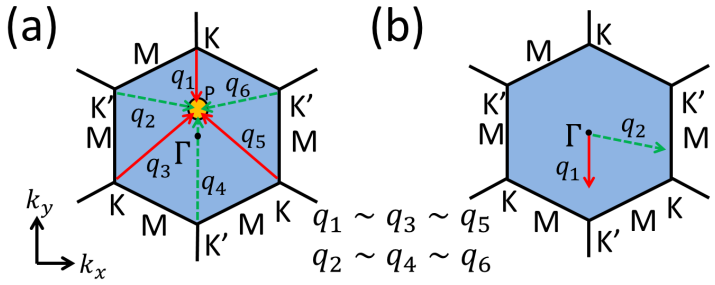

Figure 4-6: (a) Electrons are scattered from around K or K' point into a $\mathbf{k}$ point, P, shown in yellow dot, along Γ–K by phonons. The phonon wave vectors which scatter electrons from K and K' into the observation point, P, are shown by red and green dot arrow, respectively. (b) The phonon wave vector $\mathbf{q}_1, \mathbf{q}_3, \mathbf{q}_5$ and $\mathbf{q}_2, \mathbf{q}_4, \mathbf{q}_6$ indicate scattering from K and K' respectively. (d) Only two phonon momenta are nonequivalent, whereas the phonon momenta $\mathbf{q}_3, \mathbf{q}_5$ and $\mathbf{q}_4, \mathbf{q}_6$ are folded back into the first Brillouin Zone, $\mathbf{q}_1$ and $\mathbf{q}_2$, respectively, due to the lattice symmetry [11].

phonon momenta are equivalent whereas the phonon momenta $\mathbf{q}_3, \mathbf{q}_5$ and $\mathbf{q}_4, \mathbf{q}_6$ are folded into the first Brillouin zone $\mathbf{q}_1$ and $\mathbf{q}_2$, respectively, due to the lattice symmetry [11], see Fig. 4-6 (b). As a result, when the ARPES intensity along the Γ–K direction is investigated, the phonon Γ–K' and K–M–K' can be observed. Similarly, when the ARPES intensity along the Γ–K' direction is investigated, the phonon along the Γ–K and K'–M–K can be observed. Thus, we can distinguish whether the electrons scatter from K or K' points by observation of the Γ–K' or K–M–K' phonon dispersions, respectively.

b) The selection rules: the optical and lattice vibration transition rules [68] impose nonzero ARPES intensity satisfying

$$\Gamma_f \subset \Gamma_q \otimes \Gamma_m \otimes \Gamma_o \otimes \Gamma_i \tag{4.2}$$

where Γ_i, Γ_m, Γ_f, Γ_o, Γ_q are, respectively, irreducible representations for the initial state, intermediate state, final state of the electron wave function, the dipole vector and the phonon mode symmetry. The calculated symmetry of the electron state for different bands, which are important for our discussion, is shown in Fig. 2(a) graphene (b) graphite. Since the observation line is along K–Γ and K'–Γ, the mirror plane is aligned with $\sigma_v'(yz)$.

The π band as the initial state, Γ_i of the electron has to have B_2 or A_2 symmetry, as

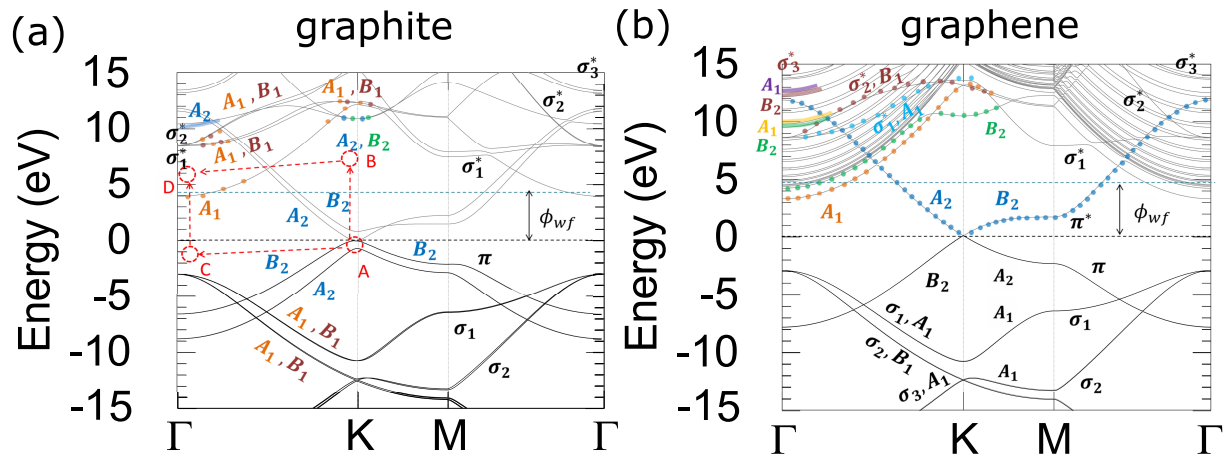

Figure 4-7: Electronic energy dispersions of (a) graphite and (b) graphene are calculated by first-principles calculations and plotted along the high symmetry points Γ–K–M–Γ up to 15 eV. In panel (a), the two possibilities of indirect transitions (A $\rightarrow$ B $\rightarrow$ D and A $\rightarrow$ C $\rightarrow$ D) are shown by the red dash-dotted arrows, in which an electron from the initial state A can reach the final state D mediated by electron-phonon interaction. The separation between the states A and B (or C and D) is determined by the incident photon energy used in ARPES (in this picture it is $\sim$ 7 eV). Note that in both panels (a) and (b) we show some symmetry representations for the energy bands which might be involved in the indirect transitions in graphene and graphite.

shown in Fig. 3-3,

$$\Gamma_i = A_2 \quad \text{or} \quad B_2. \tag{4.3}$$

The lowest conduction band near the Γ point shown with orange dots has A_{1g} symmetry at the Γ point and A_1 symmetry along the Γ–K for both graphene and graphite. The symmetry and atomic wave function of this band resemble to σ_3 which has A_{1g} symmetry at the Γ point, and A_1 symmetry along the Γ–K. We project the wave function of this state on the atomic orbital basis; this projection also verifies that this state has s orbital shape ($Y_\ell^m(\theta,\phi)$ with $\ell = 0$ and $m = 0$) near the Γ; while this state near the K point is formed by s, p_x, p_y orbitals. We call this band in this paper, A_1 band. The second lowest conduction band near the Γ point for graphene shown in Fig. 2(a) with green dots has A_{2u} symmetry at the Γ point and B_2 symmetry along the Γ–K. This band has the same symmetry in comparison with π band at the Γ point and along the Γ–K [70, 71]. Furthermore, the projection of the wave function of this band on atomic basis around Γ and K point confirms that this band is formed by

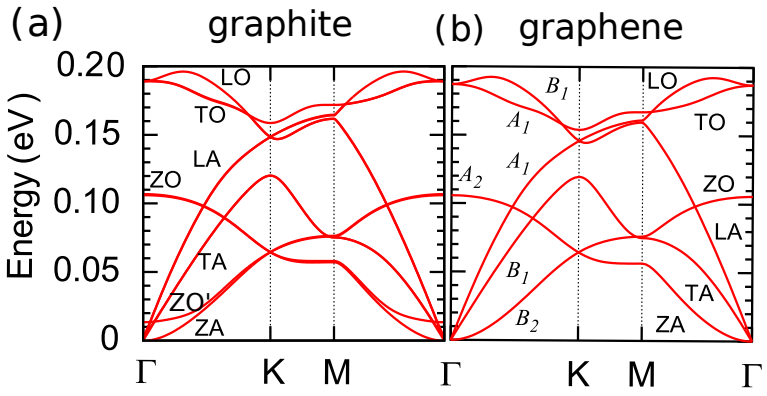

Figure 4-8: The phonon energy dispersion relations for (a) graphite and (b) graphene, obtained from first-principles calculations and density functional perturbation theory [32]. Since there is C_{2v} symmetry along the Γ–K–M and Γ–M directions, each phonon mode is labeled by the irreducible representation of the C_{2v} point group along Γ–K–M direction [72].

the p_z orbital ($\ell = 1$ and $m = 0$) near Γ and K points. In graphite, the conduction bands with energy ≈ 11 eV around the K point have A_2 and B_2 symmetry. The projection of their wave function also shows that they are formed by the p_z orbital. The σ_1^* and σ_2^* conduction bands at the Γ have the E_{2g} and E_{1u} symmetry for graphite and E_{1u} for the graphene. The σ_1^* and σ_2^* along the Γ–K have A_1 and B_1 symmetry for graphene and graphite. The σ_3^* has A_{1g} symmetry at the Γ point and A_1 symmetry along Γ–K. This band has s shape.

Since most of the phonon branches of graphite are nearly double degenerate and almost similar to graphene, in following symmetry discussion, we will use the symmetry of the phonon in graphene for simplicity [50]. Graphene has six phonon modes as shown in Fig. 4-8(b). The four in-plane phonon modes TA, LA, TO and LO along Γ–K–M transform as B_1, A_1, A_1 and B_1, respectively. The-out-of-plane phonon modes ZA and ZO along Γ–K–M transform as B_2 and A_2 respectively [73, 39, 50]. Moreover, the parity under the $\sigma_v'(yz)$ reflection along the Γ–K line are odd for TA, LO, ZO and are even for ZA and LA, TO. Since the parity of phonon modes does not change at the Γ point and along the Γ-K [51], we show the parity of graphene phonon modes at the Γ point in Fig. 4-9..

c) Conservation of parity under reflection: imposes that the integral of the $\langle f|H'|m\rangle\langle m|H'|i\rangle$ must be an even function under reflection with respect to the mirror plane which was defined in Fig. 1(a). Furthermore, the final state has to have even symmetry w.r.t the mirror plane in ARPES [22, 6, 69, 8]. Thus, The final state can be either B_2 or A_1. Eventually, we have

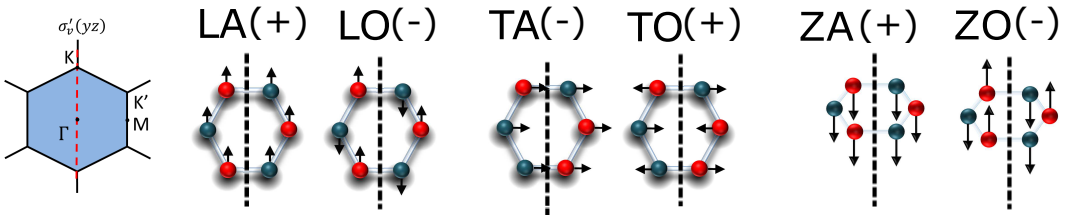

Figure 4-9: Honeycomb lattice phonon eigenvector at the Γ point, with their polarization defined with respect to the Γ–K. The mirror planes σ_v' (that leaves Γ–K invariant) are presented as the dashed lines. The parity of each phonon under the corresponding reflection is indicated in parenthesis [51]. phonon with odd (-) parity are not observed.

Table 4.3: Product table of C_{2v} representation for the indirect transition for the first process $A \to B \to D$, Γ_i indicates the initial states $\Gamma_i = \{A_2, B_2\}$, $\Gamma_o\{A_1, B_1, B_2\}$ refers the optical transition and Γ_q assigns the phonon eigenvector symmetry along Γ–K–M. the final states $\Gamma_f = \{A_1, B_2\}$ shows the symmetry of the allowed final state.

Γ_i	Γ_o(Pol.)	Γ_m	Γ_q(Ph.)	Γ_f
B_2	$A_1(p)$	B_2	A_1(TO,LA)	B_2
B_2	$B_2(p)$	A_1	A_1(TO,LA)	A_1
B_2	$A_1(p)$	B_2	B_2(ZA)	A_1
B_2	$B_2(p)$	A_1	B_2(TO,LA)	B_2
A_2	$B_1(s)$	B_2	A_1(TO,LA)	B_2
A_2	$B_1(s)$	B_2	B_2(ZA)	A_1

to mention that the p-polarized and s-polarized light transform as B_2, A_1 and B_1 symmetry.

Finally, the discussion of the selection rules is summarized in the Table 4.3. It is seen that the dispersion relation of the TO, LA and the ZA phonon modes of graphene and graphite which have even symmetry with respect to a mirror plane, can be extracted from the symmetry viewpoint.

Chapter 5

Photon energy dependent of ARPES in graphene

In this chapter, we presents our result for the direct transition. We will compare the experimental measurement and theoretical calculation of the ARPES intensity near the K point and along the Γ–K and K–M for π and π^* bands. is changed by using different photon energies and light polarizations.

5.1 Photon and polarization energy dependence

We calculate the wave function coefficients of graphene in terms of plane waves within first-principles approach as implemented in Quantum Espresso package [32]. We adopt the norm-conserving pseudopotential with Perdew-Zunger (LDA) exchange-correlation scalar relativistic functional. The kinetic energy cut-off is taken as 60 Ry for each atom and the kinetic energy cut-off for density potential is set 600 Ry in order to verify the convergence of all wave functions. The k-point mesh grid for self-consistent calculation is $52 \times 52 \times 1$ in the graphene Brillouin zone. The lattice parameter of graphene is 4.602 a.u. and the lattice constant for unit cell normal to graphene planes is taken as $c/a = 10$ to avoid interlayer interaction.

In Fig. 5-1, we show the calculated energy band structure of graphene along the high symmetry points in the first Brillouin zone of graphene. The energy dispersions are calculated

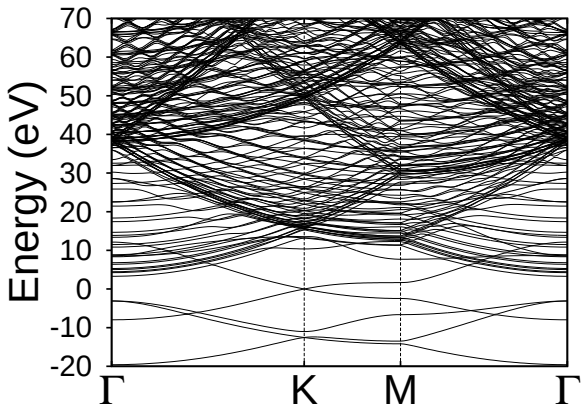

Figure 5-1: The electronic energy dispersion relation of graphene obtained from first-principles calculation is plotted along the high symmetry points Γ–K–M up to 70 eV.

up to 70 eV above the Dirac point. As seen in Fig. 5-1 the energy bands of graphene cross each other around 20 eV and 50 eV near the K point, consistent with some earlier studies [10, 8].

To investigate the photon energy dependence of graphene bands ARPES intensity near the Fermi level, the ratio of the p-branch intensity to the s-branch intensity, I_p/I_s, is measured and calculated as a function of photon energy at the Fermi level, as shown in Fig. 5-2 (The taken I_s and I_p points are shown in the inset of Fig. 5). The Dirac point is located at about -0.4 eV below the Fermi energy. The polarization angle of light is fixed to be $\phi = 80°$ and the incident angle is $\psi = 18°$ for the photon energies in the range of $\hbar\omega = 42$ eV to 55 eV. In Fig. 5-2, the circles denote the experimental measurement, while the solid line denotes the calculated result. For the polarization angle $\phi = 80°$, which is close to $\phi = 90°$ (s-polarization), it is expected that the intensity of the s-branch (A_2) is stronger than the p-branch (B_2). However, our study shows that I_p increases more significantly near $\hbar\omega = 46$ eV rather than I_s. The drastic change in the intensity ratio I_p/I_s near $\hbar\omega = 46$ eV indicates such an enhancement of the p-branch intensity. Moreover, the experimental values of I_p/I_s are larger than the theoretical values. We believe that the discrepancy might arise from our experimental setup. Since the photoelectron detection efficiency for the s-polarization is smaller than that for the p-polarization, we expect that the detection efficiency of I_s is smaller than I_p. Particularly, when I_p increases, the difference between the experimental observation and the theoretical calculation also increases. A more detailed comparison between the experimental and calculation results are shown in Fig. 5-3. In Figs. 5-3(a) and (b), we show

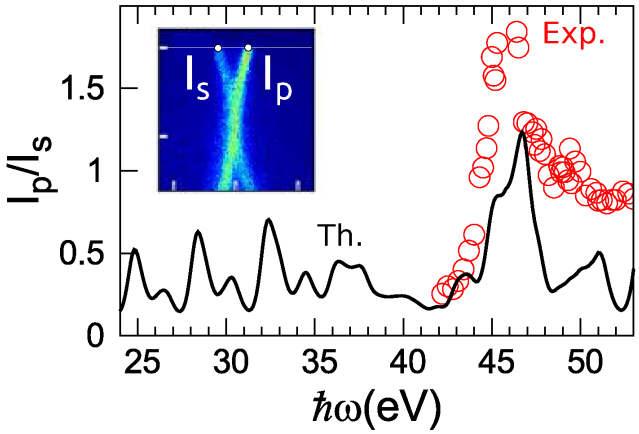

Figure 5-2: The ratio of the p-branch intensity to the s-branch intensity (I_p/I_s) is plotted as a function of photon energy $\hbar\omega$. The polarization angle is fixed at $\phi = 80°$. Open circles represents the experimental results, while the solid line represents the calculated I_p/I_s. The initial state $E_i = 0.4$ eV above the Dirac point is considered in the calculation. Both the experimental measurement and the theoretical calculation have a sharp peak around 46 eV. Inset shows a particular example how I_s and I_p (given by two dots) are taken along the s-branch and p-branch, respectively, at a given photon energy $\hbar\omega = 50$ eV.

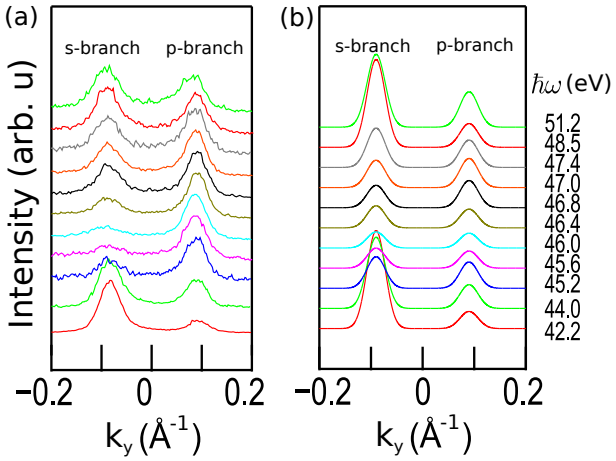

Figure 5-3: (a) Experimental and (b) calculated result of ARPES intensity (I_s and I_p) as a function of the wave vector k_y along Γ–K–M direction for several photon energies. In both experimental measurement and theoretical calculation, the light polarization angle $\phi = 80°$ and the incident light angle $\psi = 18°$ are considered. For each photon energy, the I_s and I_p values are normalized to the largest value between the two. Furthermore, $\Delta k = 0.1$ angstrom is considered to plot the intensity as a function of the wave vector.

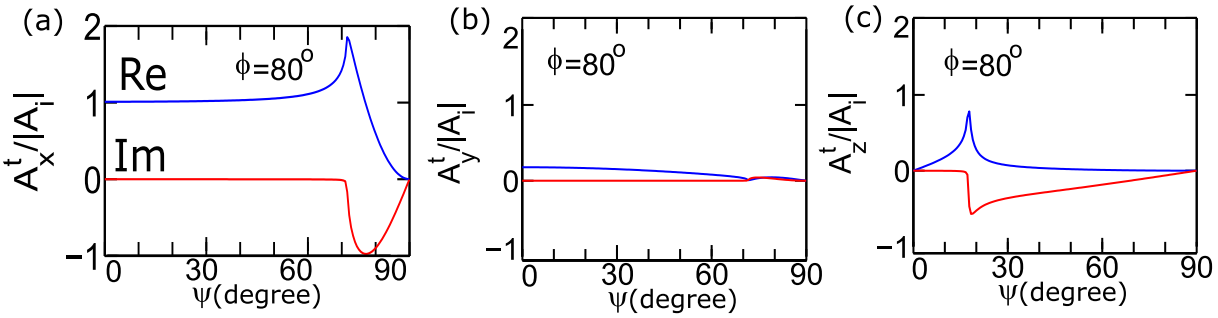

Figure 5-4: The real part and imaginary part of transmitted vector potential components: (a) A_x^t, (b) A_y^t and (c) A_z^t, plotted s a function of the incidence angle, ψ, for the light polarization angle $\phi = 80°$.

both I_p and I_s from experiment and calculation along Γ–K–M direction for several photon energies. For a given photon energy and polarization angle, I_p (I_s) is normalized to the maximum intensity values along the p-branch (s-branch) as shown in the inset of Fig. 5-2. The graphene is slightly n-doped because of charge transfer from the substrate. The Dirac point is located at about -0.4 eV below the Fermi level. It can be seen that around the photon energy of 45–48 eV the intensity of p-branch is higher than the intensity of s-branch.

The origin of enhanced intensity of p-branch near the photon energy $\hbar\omega = 46$ eV can then be explained by the electron-photon matrix element effects in graphene. Since the light incident angle is not perpendicular to the graphene surface, the vector potential outside of graphene relates to the transmitted vector potential into the graphene by Eq. (7), which is a function of the light incident angle and the dielectric function of graphene. The x, y, z component of the transmitted vector potential $\mathbf{A}$ is plotted as a function of incident light angle in Fig. 5-4 with the polarization angle of light $\phi = 80°$. It can be seen from Figs. 5-4(a) and (b) that the transmitted vector potential have values for its x- and y-components even for $\psi = 0°$, and that their real and imaginary part are almost constant for $\psi < 30°$. Meanwhile, as shown in Fig. 5-4(c), the value of the z-component of transmitted vector potential is zero. Increasing the angle ψ will give the stronger A_z. The z-component of the vector potential can enhance the intensity of p-branch (B_2) by brightening the z-component of dipole vector when the incident light is not normal to the surface.

To discuss the final state dependence of the dipole vector, we plot in Fig. 5-5 the absolute value of the dipole vector components as a function of the final state energy for different k-

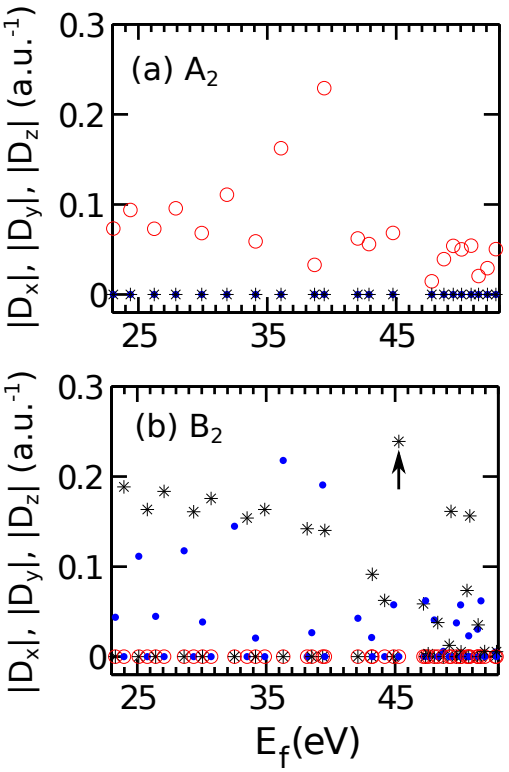

Figure 5-5: The x-, y-, and z- components of the dipole vector, i.e. D_x (circles), D_y (dots), D_z (asterisks), plotted as a function of the energy of the final state E_f. The initial energy is taken to be $E_i = 0.4$ eV. In (a), the symmetry of the initial state along Γ–K is A_2, while in (b), the symmetry of the initial state along K–M is B_2. Around 46 eV, the strong z-component of the dipole vector (as indicated by the arrow) results in a larger increase of the ARPES intensity of the p-branch compared to that of the s-branch in the presence of $\phi = 80°$ light polarization.

points near the Dirac point along Γ–K and K–M lines, which satisfy the explained symmetry rule discussed in the Sec. IV [74]. The initial state energy is $E_i = 0.4$ eV. The circles, dots, and asterisks in Fig. 5-5 denotes the x-, y-, and z- component of the dipole vector, i.e, D_x, D_y, and D_z, respectively. In our calculation, the direction of dipole vector for $\pi - \pi^*$ transition ($B_2 - A_2$), D_x, is consistent with the results from Grüneis *et al.* for the dipole vectors along the Γ–K and K–M lines [23]. The dipole vector direction for each final state can be only in one direction of x, y or z (see Fig. 5-5). Thus, the linearly-polarized light cannot break the mirror symmetry rules in the observation of photoexcited electrons, which is also confirmed by experimental measurement.

A large D_z is seen in Fig. 5-5 in the B_2 branch, around 46 eV, while the D_y values are very small near the photon energy $\hbar\omega = 46$ eV. Hence, the dependence D_y on the photon energy almost disappears, while D_z has large enhancement of the intensity for the p-branch near $\hbar\omega = 46$ eV as indicated by the arrow in Fig. 5-5(b). Therefore, when the z-component of the vector potential has a non-negligible value, the z-component of the dipole vector gives the contribution to enhancing the p-branch. For this reason, the intensity of the p-branch in graphene becomes much stronger than that of the s-branch for the photon energy near $\hbar\omega = 46$ eV. Consequently, the origin of the strong peak observed around 46 eV corresponds to the final state effects on the electron-photon interaction in graphene. Moreover, since the direction of the dipole vector does not depend on the light polarization, our study suggests that near the $\hbar\omega = 46$ eV the circular light dependency of ARPES intensity should almost disappear due to the small D_x and D_y values compared to the D_z value [24].

Chapter 6

Phonon-assited indirect of ARPES in graphene and graphite

In this Chapter, we will show our calculated result of the indirect transition. We will compare the experimental measurement for HOPG ARPES spectra near the Γ point with the theoretical calculation for graphene and graphite. We will discuss about the transition mechanism, resonant and nonresonant, for different photon energies. Furthermore, we will assign the phonon modes which can be involved and observed through the indirect transition ARPES spectra. Finally, we will explore the polarization dependence of the indirect transition for the single crystal of the graphite, experimentally and theoretically.

6.1 Phonon-assited indirect transition

To investigate the observation of the ARPES spectra at the Γ point and near the Fermi level energy, we calculate here the indirect transition ARPES intensity as a function of the binding energy, for the $\mathbf{k}$ vectors very close to the Γ point, at $\mathbf{k} = \frac{2\pi}{a} \times 10^{-4}$, along Γ–$K$ for several photon energies of graphene and graphite. Here, we consider the p-polarized light with an incident angle $\psi = 40°$. The, calculated results can then be compared with the experimental ARPES spectra.

Figure 6-1(a) shows the experimental ARPES intensity as a function of the binding energy for highly-oriented pyrolytic graphite (HOPG), whereas Figs. 6-1(b) and (c) show the

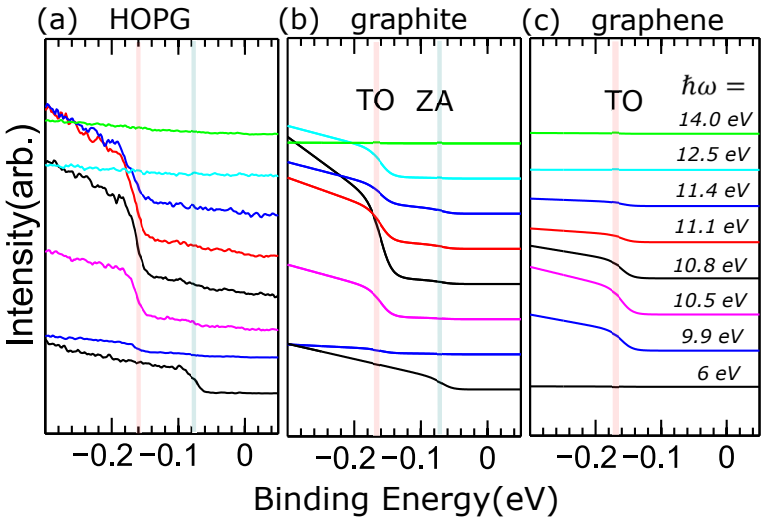

Figure 6-1: (a) The experimental ARPES intensities for HOPG compared with the calculated ARPES intensities for (b) graphite and (c) graphene near the Γ point for several incident photon energies. The incident photon is p-polarized light and the incident angle is $\psi = 40°$. In (a), step-like features are found at the binding energy $E_b \approx 154$ meV (red bar) and $E_b \approx 67$ meV (blue bar), which are assigned to the TO and ZA modes, respectively. In (b), the step-like features from the calculations for the TO and ZA modes are found to be at $E_b \approx 160$ meV and $E_b \approx 67$ meV, respectively. In (c), from our calculation, we find only the TO mode, but no ZA mode.

calculated the ARPES intensity for graphite and graphene, respectively. Looking at Figs. 6-1(a) and (b), the calculated ARPES intensity basically reproduces the experimental data. We can see that there are step-like features in the ARPES intensity at the binding energies $E_b \approx 154$ meV and $E_b \approx 67$ meV for the experimental measurements and at $E_b \approx 160$ meV and $E_b \approx 67$ meV for the corresponding theoretical calculations for graphite. The small discrepancy between the experiment and theory for the positions of step-like features might originate from the Kohn anomaly [30], which is neglected in our calculations for simplicity. We assign the step-like features at $E_b \approx 154$ meV (or 160 meV) and at $E_b \approx 67$ meV to the TO and ZA modes, respectively. Furthermore, in Fig. 6-1(c), we can see the step-like features only at $E_b \approx 160$ meV and there is no such one at $E_b \approx 67$ meV. In the present work, we only perform the calculations for graphite and monolayer graphene. However, for the TO mode, we expect that the ARPES intensity in the case of few-layer graphene might show similar results to that of graphite. As for the ZA mode, few-layer graphene might show a transition from the feature of monolayer graphene to graphite. We will understand all

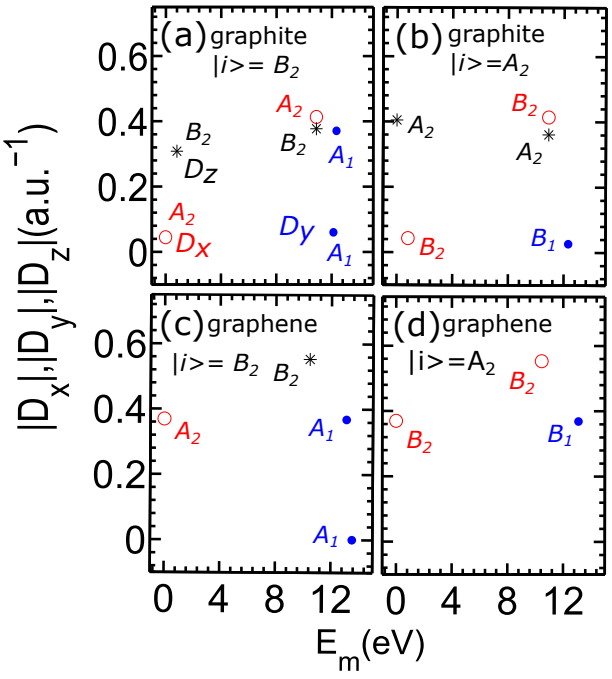

Figure 6-2: The x-, y-, and z- components of the dipole vector, i.e., D_x (circles), D_y (dots), D_z (asterisks), plotted as a function of the energy of the intermediate state (E_m) for (a) graphite with B_2 symmetry as the initial state, (b) graphite with A_2 symmetry as the initial state, (c) graphene with B_2 symmetry as the initial state, and (d) graphene with A_2 symmetry as the initial state. Symmetry labels near the circles, dots, and asterisks correspond to the symmetry of the intermediate states.

these behaviors by discussing the detailed scattering processes in the following subsections.

6.1.1 Resonant indirect transitions

For the photon energy range of 10–15 eV, it is possible to obtain a resonance process, and thus the ARPES intensity for the A $\rightarrow$ B $\rightarrow$ D transition [see again Fig. 3-3(a)] is 10 times larger than that for the A $\rightarrow$ C $\rightarrow$ D transition. In this case, the first step of the A $\rightarrow$ B $\rightarrow$ D transition is the direct optical transition, A $\rightarrow$ B, from the carbon π band to the conduction bands around the K point. For this purpose, in Fig. 6-2, we show the absolute value of the dipole vector, $\mathbf{D}(\mathbf{k}) = \langle m\mathbf{k}|\nabla|i\mathbf{k}\rangle$, as a function of the intermediate state energy for different conduction bands in graphite [Figs. 6-2(a) and (b)] and graphene [Figs. 6-2(c) and (d)]. For the initial states that satisfy Table II, we plot the dipole vectors for $|i\rangle = B_2$ [Figs. 6-2(a) and (c)] and for $|i\rangle = A_2$ [Figs. 6-2(b) and (d)]. The wave vector of the initial state of the

electron is considered at a point with a distance of $\frac{2\pi}{a} \times 10^{-4}$ from the K point along the Γ–K line. The circles, dots, and asterisks denote the x-, y-, and z- components of the dipole vectors, i.e., D_x, D_y, and D_z, respectively. The symmetry of each intermediate state is also labeled.

More detailed information about the dipole vectors plotted in Figs. 6-2(a)-(d) can be obtained by comparing them with the electronic band structures in Figs. 3-3(a)-(b). The two lowest energy optical transitions around $E_m \approx 1$ eV shown in Figs. 6-2(a) correspond to the $\pi \rightarrow \pi^*$ transitions of graphite. Next, the optical transition around $E_m \approx 11$ eV may originally correspond to the $\pi \rightarrow B_2$ or the $\pi \rightarrow A_2$ transition, since either choice is possible following Fig. 3-3(a). However, the $\pi \rightarrow A_2$ optical transition can be excluded by the selection rule in Table 4.3. At $E_m \approx 12$ eV, the intermediate state can be the A_1, or σ_1^* or σ_2^* bands (see Fig. 2). The nonzero value of the dipole vector corresponds to D_y for the $B_2 \rightarrow A_1$ transition, while the dipole vector becomes $\mathbf{D} = 0$ for $A_2 \rightarrow A_1$. The σ_1^* and σ_2^* bands as the intermediate states have A_1 and B_1 symmetries. The dipole vector for the $B_2 \rightarrow B_1$ and $A_2 \rightarrow B_1$ transitions are $\mathbf{D} = 0$ and D_y, respectively.

In Figs. 6-2(c) and (d), we show similar properties with those in Figs. 6-2(a) and (b), but now for the case of graphene. The direction of the dipole vector for $\pi \rightarrow \pi^*$ transition at $E_m \approx 0$ eV along the Γ–K and K–M is D_x, which is consistent with the results from Grüneis *et al.* [23]. The $\pi \rightarrow B_2$ transition takes place at $E_m \approx 11$ eV and the dipole vector components for this transition are D_z and D_x, as shown in Figs. 6-2(c) and (d). In the case of the third and fourth lowest conduction bands in graphene, the band with A_1 symmetry (orange dots in Fig. 3-3 around the K point) and σ_1^* band with A_1 symmetry are both involved in the electron-photon excitation. The directions of the dipole vector for the $\pi \rightarrow A_1$, and $\pi \rightarrow \sigma_1^*$ transitions along the Γ–K directions and K–M are denoted by D_y and D_x, respectively.

The electron-phonon matrix element calculation reveals that, although the TO and LA phonon modes have the same symmetry (A_1), the matrix element for the LA phonon mode near the K point is negligibly small. The insignificant electron-phonon interaction for the LA phonon mode near the K point physically originates from the direction of atomic displacements of the LA mode [75]. In Figs. 6-3(a)-(f), we show the calculated electron-phonon

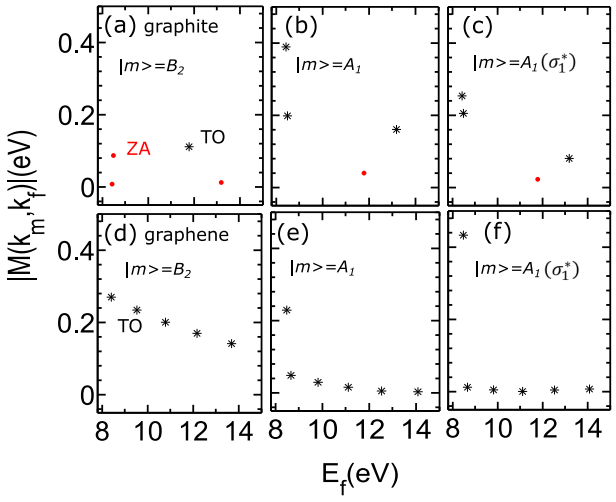

Figure 6-3: The electron-phonon matrix elements for the scattering events from the intermediate states $|m\rangle$ with particular symmetries (B_2 and A_1) into some final states with different energies E_f. Panels (a)-(c) are for graphite, while panels (d)-(f) are for graphene. The dots and asterisks refer to the electron-phonon interaction for ZA and TO phonon modes, respectively. Note that $|m\rangle$ in panels (b)-(c) and (e)-(f) have the same symmetries but originate from different bands. In particular, (c) and (f) are related with $|m\rangle$ of the σ_1^* band.

matrix elements as a function of the final state energy, E_f, in graphite and graphene. The dots and asterisks correspond to the coupling of the photoexcited electron with the ZA and TO phonon modes, respectively. The difference between graphene and graphite is physically related to the ZA phonon mode, which cannot (can) be observed in the ARPES spectra for graphene (graphite), because graphene does not have interlayer electron-phonon interaction [76]. Besides, the value of the electron-phonon matrix element decreases with increasing E_f.

For the incident photon with $\hbar\omega \approx 11$ eV, photoexcited electrons in the B_2 band are scattered into the final states near the Γ point (see Fig. 2). In the case of graphite, final states can be π^*, σ_1^* or σ_2^*. As shown in Figs. 6-3(a) and (d), the most dominant ARPES intensity for the $\hbar\omega \approx 11$ eV arises from the coupling between the photoexcited electron and the TO phonon. From these facts, we can conclude that the ARPES intensity around 154 meV for $\hbar\omega \approx 11$ eV is due to the photoexcitation from the π band to the B_2 band and then the scattering of the photoexcited electron by the TO phonon mode into a state near the Γ point. It should be noted that the discrepancy between the experimental and theoretical binding energy might come from the effect of the electron-electron correlation on

the phonon dispersion [77], which is beyond the scope of this work. For $\hbar\omega \approx 13$ eV, the intermediate state can be associated with A_1, σ_1^* or and σ_2^* bands. In this case, both the ZA and TO phonon modes can be coupled with the photoexcited electron. However, the electron-phonon interaction for the ZA phonon mode is weaker than that for the TO phonon mode as discussed above. Thus, the ARPES intensity observed for $\hbar\omega \approx 12.5$ eV is assigned to the TO and ZA phonon modes.

6.1.2 Nonresonant indirect transition

Now we consider the case when the incident photon energy is $\hbar\omega \approx 6$ eV. The excitation process is the nonresonant indirect transition and the final state is the A_1 band, which is a nearly free-electron state. Let us again discuss the possibilities of A $\rightarrow$ B $\rightarrow$ D and A $\rightarrow$ C $\rightarrow$ D transitions. If we assume that the virtual state comes from the closest real states of the electrons, the optical excitation in the second process ($\sigma_1, \sigma_2 \rightarrow A_1$) has a negligible intensity [78]. Furthermore, the optical transition along the high symmetry points on the Γ–A line (perpendicular to the Γ–K–M–Γ plane) for the second process also has a negligible intensity. Thus, the dominant mechanism should be the $A \rightarrow B \rightarrow D$ transition. As we mentioned before, although we find that the A $\rightarrow$ B $\rightarrow$ D transition would also be more preferable for $\hbar\omega \approx 6$ eV, the physical origin why this transition is dominant for $\hbar\omega \approx 6$ eV is different from that for $\hbar\omega \approx 11.1$ eV.

We can see that for the $A \rightarrow B \rightarrow D$ transition with $\hbar\omega \approx 6$ eV, the intermediate state is the B_2 band and the dominant dipole vector is D_z (see Fig. 6-2). Therefore, only the ZA phonon mode can be involved in this process (see Table 4.3). The electron-phonon matrix element as a function of the final state is plotted in Fig. 6-4. It can be seen that there is a strong coupling between the π^* band and the A_1 band [79, 80]. We conclude that the ZA phonon mode corresponds to the ARPES signal at $E_b = 67$ meV if photons with $\hbar\omega \approx 6$ eV and p-polarization come to the graphite surface.

When we look at the ARPES intensity for $\hbar\omega \approx 6$ eV and $\hbar\omega \approx 12.5$ eV in Fig. 5, there is a discrepancy between the experimental data of the ARPES intensity and the calculated results. The experimental ARPES intensity is higher than the calculated intensity for $\hbar\omega \approx 6$ eV, while the experimental ARPES intensity is much smaller than the calculated intensity

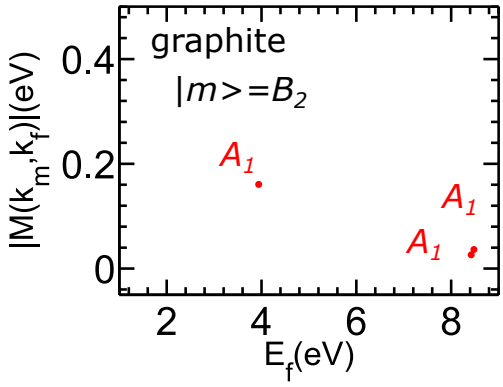

Figure 6-4: Electron-phonon matrix elements for the ZA phonon mode of graphite for the transitions from an intermediate state $m\rangle$ having B_2 symmetry (the π^* band near the K point) into some different final states with energies E_f.

Table 6.1: Phonon ($|Ph\rangle$) assignment for different photon energies ($\hbar\omega$). Columns for $|i\rangle$, $|m\rangle$ and $|f\rangle$ show the orbital shapes for initial, intermediate, and final states, respectively, while $|O\rangle$ denotes the direction of the dipole vector.

$\hbar\omega(eV)$	$\|i\rangle$	$\|O\rangle$	$\|m\rangle$	$\|Ph\rangle$	$\|f\rangle$
6	p_z	D_z	p_z	ZA	s
11	p_z	D_z,D_y	p_z	TO	p_z
13	p_z	D_y	s, p_x, p_y	TO	s

for $\hbar\omega \approx 12.5$ eV. The origin of this discrepancy might be explained by the angle between the emission direction of the ejected photoelectron and the detector [11]. The direction of the detector is considered to be normal to the surface in the experiment [11, 12]. In Table 6.1, we show the shapes of the orbitals for the initial state $|i\rangle$, the intermediate state $|m\rangle$, the final state $|f\rangle$, the dipole vector direction, $|O\rangle$, and the phonon polarization, $|Ph\rangle$, for photon energies $\hbar\omega = 6$ eV, 11 eV and 13 eV. Every initial state is the π electron band, formed by the p_z orbital. For the $\hbar\omega \approx 6$ eV transition, the $|m\rangle$ also has the p_z orbital character. The dipole vector becomes D_z and the out-of-plane phonon mode ZA also couples to the photoexcited electron. In this case, the final state, $|f\rangle$, has an s orbital shape. Therefore, the ejected electron from this excitation process can be observed in the direction normal to surface more dominantly. For the $\hbar\omega \approx 11$ eV excitation, the $|m\rangle$ also has p_z shape and the dipole vector also becomes D_z. However, in this case, the electrons couple to the in-plane phonon mode TO and $|f\rangle$ has p_z shape. As a result, the ejected electrons from this process also can be well-observed in the direction normal to the surface. But we should note that the

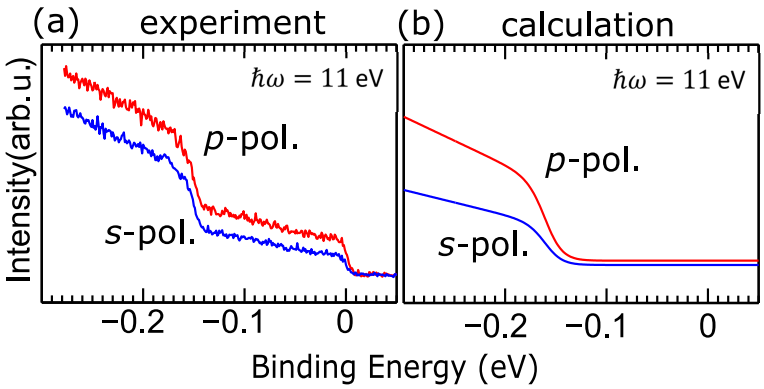

Figure 6-5: (a) Experimental measurement and (b) theoretical calculation of the ARPES intensity as a function of the binding energy. The energy of the incident photon is $\hbar\omega = 11$ eV. The higher and lower curves correspond to the ARPES intensity for s-polarized and p-polarized light, respectively.

intensity of the observed electrons can decrease due to the coupling between the electron and the phonon mode. For the $\hbar\omega \approx 12.5$ eV, the intermediate state has s, p_x, p_y orbital shapes and the dipole vector is D_y and also the electron is coupled with the in-plane TO phonon mode, and in this case the final state has an s orbital shape. The ejected electrons from this process thus have a large dipole vector component parallel to the surface so that the possibility of the observation of the electrons from this process when the detector is normal to the surface will dramatically decrease.

6.1.3 Effects of s- and p-polarizations

Finally, we discuss the polarization dependence of the incident light. In figures. 6-5 (a) and (b), we plot the experimental and calculation data of graphite for the s-polarized and p-polarized light for $\hbar\omega = 11$ eV. It can be seen that the ARPES intensity for p-polarized light is stronger than s-polarized light for both experimental measurement and theoretical calculation. It is because that the z-component of the vector potential (A_z) is stronger than the $x-$component (A_x) for $\hbar\omega = 11$ eV and $\psi = 40°$ although the dipole vector components D_z and D_x have the same magnitude (see Fig. 6-2).

Chapter 7

Conclusion

In this thesis, we have discussed the theoretical calculation for the ARPES in graphene and graphite and the calculated results were compared with the experimental measurements. Calculation have been performed particularly near the K point and Γ point and closed to the Fermi level which are correspond to the observation of the direct and the indirect transition ARPES spectra. In order to understand the direct and indirect ARPES spectra, we need a detailed knowledge of the electronic structure, optical matrix elements, phonon modes and electron-phonon matrix elements. In this study we drive two formula to calculate the electron-photon interaction and the electron-phonon coupling based on the plane wave wave functions. Then, we make codes to calculate them. The eigenvalues and eigenvectors of the electronic structure and phonon modes are obtained by the Quantum Espresso package. Our finding can be divided in two parts:

7.1 Direct transition of ARPES spectra

The direct transition of the ARPES spectra is studied for the electronic bands near the K point and closed to the Fermi level in graphene. We have discussed the photon energy dependence of ARPES intensity for π and π^* bands, by the ARPES measurement and first-principles calculations. Based on the measured and calculated ARPES intensity, we conclude that the intensity of the p-branch in graphene near the photon energy $\hbar\omega = 46$ eV is stronger than that of the s-branch even when the polarized light is almost parallel to

the s-polarization. The origin of this observation is explained by the effects of the electron-photon matrix elements on ARPES intensity in graphene. This study suggests that the presence of larger z-component of the dipole vector compared to the y-components results in the enhanced intensity of p-branch near $\hbar\omega = 46$ eV. Furthermore, the chiral dependence in ARPES can be explained by the group theory. This approach also confirms that the p-polarized light brightens the band with B_2 symmetry which has even symmetry with respect to mirror plane and s-polarized light brightens the band with A_2 symmetry which has odd symmetry with respect to the mirror plane.

7.2 Indirect transition of ARPES spectra

The indirect transition for the ARPES spectra in graphene and graphite have been investigated for different incident photon energies and light polarizations. Our symmetry analysis shows that the phonon modes, ZA, TO and LA, which have even symmetry with respect to the mirror plane, $\sigma_v'(yz)$, can be involved in the indirect interband transition. Although the LA phonon mode has even symmetry with respect to the mirror plane, its phonon energy cannot be observed because it has a negligible electron-phonon interaction near the K point in the Brillouin zone. Thus, the ARPES spectra with binding energy $E_b = 154$ eV is assigned to the TO phonon modes of graphene and graphite when p-polarized photons with $\hbar\omega \approx 11$ eV are used. The relevant mechanism for the observation of the TO phonon mode is a resonant indirect transition. Meanwhile, for the incident photons with $\hbar\omega \approx 6$ eV, the ZA mode becomes dominant, being observable through a nonresonant indirect transition occurring in graphite for p-polarized light. Furthermore, the ARPES intensity of graphite for p-polarized light is stronger than for s-polarized light when the incident photon energy is $\hbar\omega \approx 11$ eV because the vector potential of the p-polarized light is expected to be stronger than that of s-polarized light.

By understanding the indirect transitions in the ARPES spectra of graphite and graphene, we expect that more detailed phonon dispersion relations might be observed in our future experiments. Besides, we believe that the validity of our methods should not be limited to graphene-based materials. We may expect that the electron-phonon coupling for a large class

of two-dimensional materials should also be observable by ARPES with indirect transitions.

Appendix A

Appendix: Electron-photon dipole vector

In this section, we will describe how to calculate the electron-photon interaction matrix element by using first-order time-dependent perturbation theory and plane wave wave function for different bands.

A.1 Dipole vector

The dipole vector $\mathbf{D}(\mathbf{k}_i, \mathbf{k}_f)$ is defined as

$$\mathbf{D}(\mathbf{k}_i, \mathbf{k}_f) = \langle \Psi^f(\mathbf{k}_f, \mathbf{r}) | \nabla | \Psi^i(\mathbf{k}_i, \mathbf{r}) \rangle. \tag{A.1}$$

To consider the final state effects on the matrix elements, we expand the wave functions of the initial states and final states in terms of plane waves,

$$\begin{aligned} \Psi^i(\mathbf{k}_i, \mathbf{r}) &= \sum_{\mathbf{G}_i} C^i_{\mathbf{G}_i}(\mathbf{k}_i) \exp\Big(i\big(\mathbf{k}_i + \mathbf{G}_i\big) \cdot \mathbf{r}\Big), \\ \Psi^f(\mathbf{k}_f, \mathbf{r}) &= \sum_{\mathbf{G}_f} C^f_{\mathbf{G}_f}(\mathbf{k}_f) \exp\Big(i\big(\mathbf{k}_f + \mathbf{G}_f\big) \cdot \mathbf{r}\Big), \end{aligned} \tag{A.2}$$

where $\mathbf{G}$ are the reciprocal lattice vectors of graphene and $C^{i,f}_{\mathbf{G}}(\mathbf{k})$ are plane wave coefficients.

Hence, the dipole vector has been calculated in the plane wave basis as

$$\begin{aligned}\mathbf{D}(\mathbf{k}_f,\mathbf{k}_i) &= \sum_{\mathbf{G}_i,\mathbf{G}_i} C^{f^*}_{\mathbf{G}_f}(\mathbf{k}_f) C^{i}_{\mathbf{G}_i}(\mathbf{k}_i) \\ &\Big\langle \exp\Big(-i\big(\mathbf{k}_f+\mathbf{G}_f\big)\cdot\mathbf{r}\Big)|\nabla|\exp\Big(i\big(\mathbf{k}_i+\mathbf{G}_i\big)\cdot\mathbf{r}\Big)\Big\rangle,\end{aligned} \tag{A.3}$$

If we take the derivative from the initial state wave function, the dipole vector can be calculated as

$$\begin{aligned}\mathbf{D}(\mathbf{k}_f,\mathbf{k}_i) &= i\sum_{\mathbf{G}_i,\mathbf{G}_f} C^{f^*}_{\mathbf{G}_f}(\mathbf{k}_f) C^{i}_{\mathbf{G}_i}(\mathbf{k}_i)\big(\mathbf{k}_i+\mathbf{G}_i\big) \\ &\int \exp\Big(-i\big(\mathbf{k}_f+\mathbf{G}_f\big)\cdot\mathbf{r}\Big)\exp\Big(i\big(\mathbf{k}_i+\mathbf{G}_i\big)\cdot\mathbf{r}\Big)d\mathbf{r},\end{aligned} \tag{A.4}$$

and then

$$\begin{aligned}\mathbf{D}(\mathbf{k}_f,\mathbf{k}_i) &= i\sum_{\mathbf{G}_i,\mathbf{G}_f} C^{f^*}_{\mathbf{G}_f}(\mathbf{k}_f) C^{i}_{\mathbf{G}_i}(\mathbf{k}_i)\big(\mathbf{k}_i+\mathbf{G}_i\big) \\ &\int \exp\Big(-i\big(\mathbf{k}_f+\mathbf{G}_f-\mathbf{k}_i-\mathbf{G}_i\big)\cdot\mathbf{r}\Big)d\mathbf{r},\end{aligned} \tag{A.5}$$

where the integral is taken over all super cell and it is the definition of the delta Dirac function. Thus the dipole vector is given as

$$\mathbf{D}(\mathbf{k}_f,\mathbf{k}_i) = i\sum_{\mathbf{G}_i,\mathbf{G}_f} C^{f^*}_{\mathbf{G}_f}(\mathbf{k}_f) C^{i}_{\mathbf{G}_i}(\mathbf{k}_i)\big(\mathbf{k}_i+\mathbf{G}_i\big)\delta(\mathbf{k}_f+\mathbf{G}_f-\mathbf{k}_i-\mathbf{G}_i), \tag{A.6}$$

We set the upper limit of photon energy as 60 eV. In this case, the optical transition occurs vertically in the $\mathbf{k}$ space, that is, $\mathbf{k}_i \approx \mathbf{k}_f = \mathbf{k}$. It should be noted that this assumption is no longer valid in the XPS measurement [55].

$$\mathbf{D}(\mathbf{k}) = i\sum_{\mathbf{G}} C^{f^*}_{\mathbf{G}}(\mathbf{k}) C^{i}_{\mathbf{G}}(\mathbf{k})\big(\mathbf{k}+\mathbf{G}\big). \tag{A.7}$$

Appendix B

Appendix: Fresnel equation

In this Chapter, we will obtain the Fresnel equation which relate the incident light to the transmitted light by the incident angle of the light, its polarizations, and the electric permittivity.

B.1 Fresnel equation

In this section, we discuss how the propagation of electromagnetic radiation changes at the boundary between free space and a solid. The description of the phenomena leads to understanding of the reflectively R, the absorptive A, and transmission T in optical process. All of these quantities are directly accessible to experiments although the relation between the incident light and transmitted one is more useful [52, 53, 54]. Let us consider the propagation of a plane electromagnetic wave from a vacuum with electric permittivity $\epsilon_0 = 1$, magnetic permittivity $\mu_0 = 1$, and conductance $\sigma = 0$ into a solid with with ϵ_1 and σ_1 while the $\mu_1 = 1$ remains the same. The Maxwell equation in the vacuum is expressed as

$$\begin{aligned} \nabla^2\mathbf{E} - \mu\epsilon\frac{\partial^2\mathbf{E}}{\partial\mathbf{t}^2} = 0, \\ \nabla^2\mathbf{H} - \mu\epsilon\frac{\partial^2\mathbf{H}}{\partial\mathbf{t}^2} = 0, \end{aligned} \tag{B.1}$$

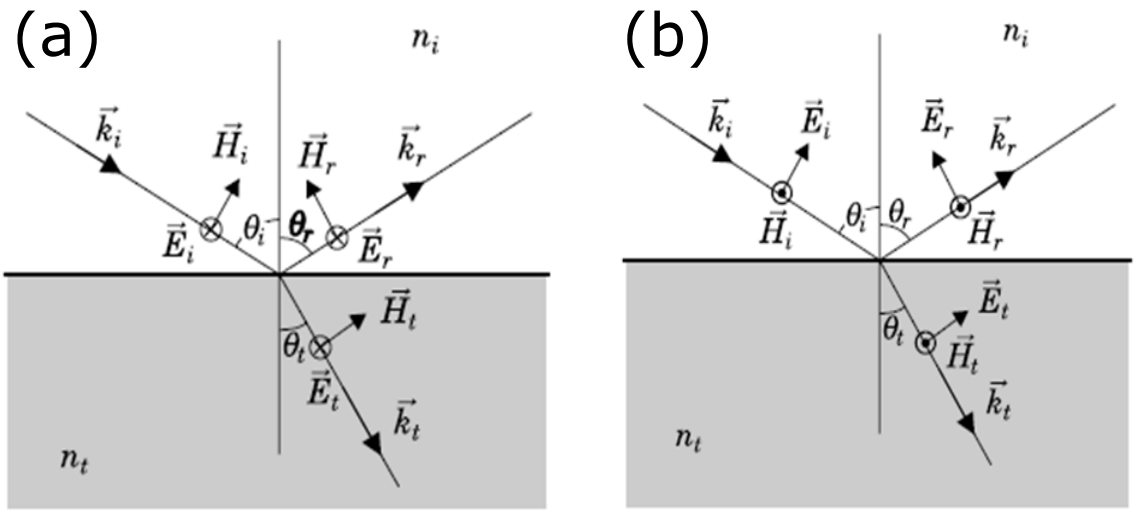

Figure B-1: (a) Field vectors of the incident, transmitted, and reflected waves in case the electric field vectors are perpendicular to the plane of incident (S polarization). (b) Field vectors of the incidence, transmitted, and reflected wave in case the electric field lie within the plane of incidence (P polarization).

thus, the incident, reflected and transmitted electromagnetic wave are

$$E_i = E_{0i} \exp\left(i\mathbf{k}_i \cdot \mathbf{r} - \omega_i t\right) E_r = E_{0r} \exp\left(i\mathbf{k}_r \cdot \mathbf{r} - \omega_r t\right) E_t = E_{0t} \exp\left(i\mathbf{k}_t \cdot \mathbf{r} - \omega_t t\right) \tag{B.2}$$

where $\mathbf{k}_i$, $\mathbf{k}_r$ and $\mathbf{k}_t$ are the incident, reflected and transmitted wave vector. First, we consider that the incident wave is S-polarized (see Fig. B-1 (a)). Since there is no charge on the surface, the boundary condition becomes:

$$\nabla \cdot \mathbf{D} = 0 \Rightarrow \mathbf{E}_i + \mathbf{E}_r = \mathbf{E}_t, \tag{B.3}$$

and

$$\mathbf{H}_{\parallel} : \mathbf{H}_i \cos\theta_i - \mathbf{H}_r \cos\theta_r = \mathbf{H}_t \cos\theta_t. \tag{B.4}$$

We know from Maxwell equations that the electromagnetic wave must satisfy the following equation:

$$\mathbf{H} = \sqrt{\frac{\epsilon}{\mu}}\mathbf{E} = \frac{1}{v\mu}\mathbf{E}, \tag{B.5}$$

where ϵ and μ are the electric permittivity and magnetic permeability, respectively, of the materials in which the wave propagates. Since the index of refraction of a material is given by $n = c\sqrt{\epsilon\mu} = c/v$, we have:

$$\mathbf{H}_{\parallel} : c\Big(\mathbf{H}_i \cos\theta_i - \mathbf{H}_r \cos\theta_r = \mathbf{H}_t \cos\theta_t\Big), \tag{B.6}$$

and using Snell's law:

$$n_i \sin\theta_i = n_t \sin\theta_t, \tag{B.7}$$

where n_i and n_t are the refractive indices of the two media and The θ_i and θ_t is the incident and transmitted electromagnetic wave function angle with respect to the normal to the surface. Note that, the θ_r angle of the reflected wave is equal to the θ_i. Combining Eqs. B.3, B.4 and B.7, we have

$$E_r^{\perp} = \frac{\cos\theta_i - \sqrt{n^2 \sin^2\theta_i}}{\cos\theta_i + \sqrt{n^2 - \sin^2\theta_i}} E_i^{\perp}, \tag{B.8}$$

and

$$E_t^{\perp} = \frac{2\cos\theta_i}{\cos\theta_i + \sqrt{n^2 - \sin^2\theta_i}} E_i^{\perp}. \tag{B.9}$$

Now, if we consider that the incident wave is P-polarized (see Fig. B-1 (b)), the boundary

condition for magnetic field becomes:

$$\mathbf{H}_i + \mathbf{H}_r = \mathbf{H}_t, \tag{B.10}$$

and for the electric field is given by

$$\mathbf{E}_i^{\parallel} : \mathbf{E}_i^{\parallel} \cos\theta_i - \mathbf{E}_r^{\parallel} \cos\theta_r = \mathbf{E}_t^{\parallel} \cos\theta_t. \tag{B.11}$$

Using the Eqs. B.7, B.10 and B.11 we get:

$$\frac{n_i}{\mu_i}\Big(E_i^{\parallel} + E_r^{\parallel}\Big)\cos\theta_i = \frac{n_t}{\mu_t}\Big(E_i^{\parallel} + E_r^{\parallel}\Big)\cos\theta_t. \tag{B.12}$$

The reflected electric field is obtained as:

$$E_r^{\parallel} = \frac{\frac{n_t}{\mu_t}\cos\theta_i - \frac{n_i}{\mu_i}\cos\theta_t}{\frac{n_t}{\mu_t}\cos\theta_i + \frac{n_i}{\mu_i}\cos\theta_t} E_i^{\parallel}, \tag{B.13}$$

and the transmitted electric field is derived as:

$$E_t^{\parallel} = \frac{2\frac{n_i}{\mu_i}\cos\theta_i}{\frac{n_t}{\mu_t}\cos\theta_i + \frac{n_i}{\mu_i}\cos\theta_t} E_i^{\parallel}. \tag{B.14}$$

Therefore, the reflected and the transmitted electric field can be written as follows:

$$E_r^{\parallel} = \frac{n^2\cos\theta_i - \sqrt{n^2 - \sin^2\theta_i}}{n^2\cos\theta_i + \sqrt{n^2 - \sin^2\theta_i}} E_i^{\parallel}, \tag{B.15}$$

and,

$$E_t^{\parallel} = \frac{2n\cos\theta_i}{n^2\cos\theta_i + \sqrt{n^2 - \sin^2\theta_i}} E_i^{\parallel}. \tag{B.16}$$

To have each component of the electric field in the x, y and z axes, we project the parallel and perpendicular component of the electric field on the x, y and z axes. For the z component

of the electric field we have:

$$E_{t,z}^{\parallel} = \frac{2n\cos\theta_i\cos(\theta_t - \frac{\pi}{2})}{n^2\cos\theta_i + \sqrt{n^2 - \sin^2\theta_i}}E_i^{\parallel} = \frac{2n\cos\theta_i\sin\theta_t}{n^2\cos\theta_i + \sqrt{n^2 - \sin^2\theta_i}}E_i^{\parallel}, \tag{B.17}$$

then

$$E_{t,z}^{\parallel} = \frac{2n\cos\theta_i\sin\theta_i}{n^2\cos\theta_i + \sqrt{n^2 - \sin^2\theta_i}}E_i^{\parallel}. \tag{B.18}$$

For the y component of the electric field, we have:

$$E_{t,y}^{\parallel} = \frac{2n\cos\theta_i\sin\theta_t}{n^2\cos\theta_i + \sqrt{n^2 - \sin^2\theta_i}}E_i^{\parallel} = \frac{2n\cos\theta_i\sqrt{n^2 - \sin^2\theta_i}}{n^2\cos\theta_i + \sqrt{n^2 - \sin^2\theta_i}}E_i^{\parallel}. \tag{B.19}$$

For the x component of the electric field, we have:

$$E_{t,x}^{\parallel} = \frac{2\cos\theta_i}{\cos\theta_i + \sqrt{n^2 - \sin^2\theta_i}}E_i^{\parallel}. \tag{B.20}$$

Appendix C

Appendix: Electron-phonon matrix elements

C.1 Atomic deformation potential

The atomic deformation potential vector is defined as follows

$$\mathbf{m}_D(\mathbf{k}_f, \mathbf{k}_i) = \int e^{i(\mathbf{k}_f - \mathbf{k}_i + \mathbf{G}' - \mathbf{G})\cdot\mathbf{r}} \nabla_{\mathbf{r}} V(\mathbf{r}') d\mathbf{r}. \tag{C.1}$$

The potential of the electrons in the field of an atom is

$$V(r) = \frac{1}{r} \sum_p v_p e^{-\frac{r^2}{2\tau_p^2}} \tag{C.2}$$

where v_p and τ_p are given by the fitting the screened potential and listed in Table 3.1. By getting integration by parts, we have

$$\mathbf{m}_D(\mathbf{k}_f, \mathbf{k}_i) = i(\mathbf{k}_f - \mathbf{k}_i + \mathbf{G}' - \mathbf{G}) \int e^{i(\mathbf{k}_f - \mathbf{k}_i + \mathbf{G}' - \mathbf{G})\cdot\mathbf{r}} V(\mathbf{r}') d\mathbf{r}. \tag{C.3}$$

If we consider $\mathbf{k}_f - \mathbf{k}_i + \mathbf{G}' - \mathbf{G} = \mathbf{Q}$, and putting Eq. C.2 into the Eq. C.3, the integral part of the atomic deformation potential is given by

$$m'_D = \sum_p v_p \int \frac{e^{-i\mathbf{Q}\cdot r'} e^{\frac{r'^2}{2\tau_p^2}}}{r'} d^3r' \tag{C.4}$$

If we just consider the integral part of the Eq. C.4 as, m''_D, we have

$$m''_D = \int_0^{2\pi} d\phi \int_0^{\pi} \int_0^{\infty} \frac{r'^2 e^{-i\mathbf{Q}r'\cos\theta} e^{\frac{-r'^2}{2\tau_p^2}}}{r'} d\cos\theta dr' \tag{C.5}$$

The angle dependence of Eq. C.5 is calculated as follows

$$m''_D = \frac{2\pi}{i|\mathbf{Q}|} \int_0^{\infty} \left(e^{i\mathbf{Q}r'} - e^{-i\mathbf{Q}r'}\right) e^{\frac{-r'^2}{2\tau_p^2}} dr'. \tag{C.6}$$

Now, we make a full square for the exponential function in Eq. C.6, by follows

$$\begin{aligned} &r'^2 - 2i\mathbf{Q}r'\tau_p^2 + (i\mathbf{Q}\tau_p^2)^2 - (i\mathbf{Q}\tau_p^2)^2 \\ &r'^2 + 2i\mathbf{Q}r'\tau_p^2 + (i\mathbf{Q}\tau_p^2)^2 - (i\mathbf{Q}\tau_p^2)^2, \end{aligned} \tag{C.7}$$

then, we have

$$\begin{aligned} -\frac{1}{2\tau_p^2}(r'^2 - 2ir'\mathbf{Q}\tau_p^2) &= -\frac{1}{2\tau_p^2}(r' - i\mathbf{Q}\tau_p^2)^2 - \frac{1}{2}(\mathbf{Q}\tau_p)^2 \\ -\frac{1}{2\tau_p^2}(r'^2 + 2ir'\mathbf{Q}\tau_p^2) &= -\frac{1}{2\tau_p^2}(r' + i\mathbf{Q}\tau_p^2)^2 - \frac{1}{2}(\mathbf{Q}\tau_p)^2. \end{aligned} \tag{C.8}$$

Therefore, m''_D, Eq. C.6, becomes

$$m''_D = \frac{2\pi e^{\frac{1}{2}(\mathbf{Q}\tau_p)^2}}{i|\mathbf{Q}|} \int_0^{\infty} \left(e^{-\frac{1}{2\tau_p^2}(r'+i\mathbf{Q}\tau_p^2)^2} - e^{-\frac{1}{2\tau_p^2}(r'-i\mathbf{Q}\tau_p^2)^2}\right) e^{\frac{-r'^2}{2\tau_p^2}} dr'. \tag{C.9}$$

If we change the variables, $z = r' + i\mathbf{Q}\tau_p^2$ and $z' = r' - i\mathbf{Q}\tau_p^2$,

$$\begin{aligned} z &= r' + i\mathbf{Q}\tau_p^2 \quad \text{if} \quad r' = 0 \Rightarrow z = -i\mathbf{Q}\tau_p^2 \quad \text{if} \quad r' = \infty \Rightarrow z = \infty \\ z' &= r' - i\mathbf{Q}\tau_p^2 \quad \text{if} \quad r' = 0 \Rightarrow z = i\mathbf{Q}\tau_p^2 \quad \text{if} \quad r' = \infty \Rightarrow z = \infty \end{aligned} \tag{C.10}$$

and considering the integral part of Eq. C.6, as m_D''', we have

$$m_D''' = \int_{-i\mathbf{Q}\tau_p^2}^{\infty} e^{-\frac{z^2}{2\tau_p^2}} dz - \int_{i\mathbf{Q}\tau_p^2}^{\infty} e^{-\frac{z'^2}{2\tau_p^2}} dz'. \tag{C.11}$$

The error function is defined as follows

$$\text{Erfi} = \frac{2}{\sqrt{\pi}} \int_x^{\infty} e^{-t^2} dt \tag{C.12}$$

thus Eq. C.11 becomes

$$m_D''' = \frac{\sqrt{\pi}}{2}\Big(\frac{1}{\sqrt{\frac{1}{(\sqrt{2}\tau_p)^2}}} + \sqrt{2}\tau_p \text{Erfi}(\frac{i\mathbf{Q}\tau_p}{\sqrt{2}}) - \frac{1}{\sqrt{\frac{1}{(\sqrt{2}\tau_p)^2}}} + \sqrt{2}\tau_p \text{Erfi}(\frac{-i\mathbf{Q}\tau_p}{\sqrt{2}}) \Big) \tag{C.13}$$

and the m_D''' becomes

$$m_D''' = \sqrt{2\pi}\Big(\tau_p \text{Erfi}(\frac{i\mathbf{Q}\tau_p}{\sqrt{2}}) \Big) \tag{C.14}$$

Finally we the atomic deformation potential is

$$\begin{aligned} \mathbf{m}_D(\mathbf{k_f}, \mathbf{k_i}) = &- i2\pi\sqrt{2\pi}\frac{\mathbf{Q}}{|\mathbf{Q}|} \times \sum_{p=1}^{4} v_p \tau_p \text{Erfi}(\frac{(|\mathbf{Q}|)\tau_p}{\sqrt{2}}) \times \\ &\exp\left(-(\frac{(|\mathbf{Q}|)\tau_p}{\sqrt{2}})^2\right) \end{aligned} \tag{C.15}$$

where $\mathbf{Q} = \mathbf{q} + \mathbf{G}' - \mathbf{G}$ and $\text{Erfi}(z)$ is the imaginary error function.

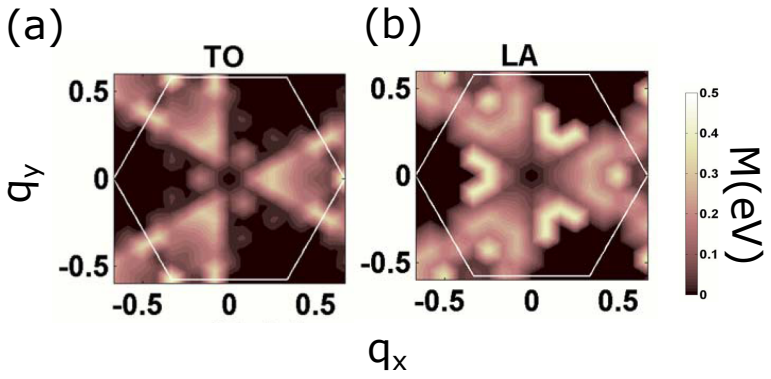

Figure C-1: Electron-phonon interaction matrix elements (in units of eV), (a) TO phonon mode, (b) LA phonon mode, are calculated by DFPT for **k** at conduction-band minimum (i.e. the Dirac point) as a function of phonon wave vector[81].

C.2 Electron LA phonon mode coupling discussion

Our calculation for the electron LA phonon mode coupling shows that the electron-phonon coupling is negligibly small for the scattering of the electron from the K point to near the Γ point by LA phonon modes because of the atomic displacements and it is independent on the electronic band structure. To investigate this acclaim we will show that the DFPT calculation for the scattering the electron from the K into the Γ point by LA phonon mode for the lowest conduction band [81].

Fig. C-1 shows the EPC matrix elements is obtained from the DFPT [81]. The initial state of the electron is considered at the direct point ($\mathbf{K} = (4\pi/3a, 0)$) of the lowest conduction band. Comparing the EPC for TO with LA phonon modes in Fig. C-1(a) and (b), respectively, near the $q \approx K$, shows that the EPC for LA phonon is much less than TO phonon mode [81].

Appendix D

Appendix: Phonon dipersion calculation in graphene by QE

In this section, we will show as an example the input file of QE to calculate the phonon dispersion relations of graphene which is included a self consistent calculation and phonon calculation. Therefore, the inputs card that in the thesis is mentioned can be clearly seen.

D.1 the self consistent calculation for graphene

The input file to calculate the self consistent calculation:

& control calculation = 'scf'

prefix='graphene',

tstress = .true.

tprnfor = .true.

pseudo_dir = ,

outdir=

/

& system ibrav = 4,

celldm(1) = 4.653048814,

celldm(3) = 4.000020191,

nat = 2,

ntyp = 1,

ecutwfc = 100.0,

ecutrho = 1200.0,

occupations = 'smearing'

smearing = 'm-p'

degauss = 0.02

/

& electrons convthr = ,

mixingmode = plain ,

mixingbeta = 0.7 ,

diagonalization = cg ,

/

ATOMIC_SPECIES

C 12.0107 C.pbe-rrkjus.UPF

ATOMIC_POSITIONS alat

C 0.00 0.00 0.00

C 0.00 0.57735026918962576451 0.00

K _POINTS

20 20 1 0 0 0

D.2 The phonon calculation for graphene

The input file to calculate phonon of graphene: & inputph

tr2_ph=1.0×10^{-10},

prefix='graphene',

epsil=.false.,

amass(1)=12.0107,

outdir=,

fildyn='graphene.dyn',

ldisp=.true.,

nq1= 6,

nq2= 6,

nq3= 1,

/

Publication list

Papers

1. **P. Ayria**, A. R. T. Nugraha, E. H. Hasdeo, T. R. Czank, S. Tanaka, R. Saito, Photon energy dependence of angle-resolved photoemssion spectroscopy in graphene. Phys.Rev.B, 92, 195148, (2015).

2. **P. Ayria**, S. Tanaka, A. R. T. Nugraha, M. dresselhaus, R. Saito, Phonon-assisted indirect transitions in angle-resolved photoemission spectra of graphite and graphene, Phys.Rev.B, Submitted (2016).

Conferences

1. **P. Ayria**, A. R. T. Nugraha, E. H. Hasdeo, R. Saito, Polarization dependence of angle-resolved photoemssion spectroscopy in graphene, ATI 2014 Nano-arbon Meeting, Yamagata-Zao, (2014.07.31-8.1).

2. **P. Ayria**, A. R. T. Nugraha, E. H. Hasdeo, R. Saito, Polarization dependence of ARPES intensity in graphene, FNTG 47 (2014.09.3-5).

3. **P. Ayria**, A. R. T. Nugraha, E. H. Hasdeo, S. Tanaka, R. Saito, Photon energy dependene of ARPES in graphene, FNTG 48 (2015.02.21-23).

4. **P. Ayria**, A. R. T. Nugraha, E. H. Hasdeo, S. Tanaka, R. Saito, Photon energy dependene of ARPES in graphene, NT15: The sixteenth international conference on the science and application of nanotubes, Nagoya Univerity, Japan (2015.06.29-07-03).

5. T.R.Czank, **P. Ayria**, R. Saito, Exciton-photon interaction in tip-enhanced raman spectroscopy of signle wall carbon nanotubes, NT15: The sixteenth international conference on the science and application of nanotubes, Nagoya University, Japan (2015.06.29-07.03).

6. Y. Tatsumi, **P. Ayria**, H. Guo, T. Yang, R. Saito, Anisotropy of optical absorption spectrum of phosphorene, FNTG 49 (2015.09.7-9).

7. **P. Ayria**, R. Saito, Selection rule of electron-phonon and electron-photon interaction observed by ARPES in graphene, 6th A3 symposium on emerging materials, Kyushu University, Fukuoka (2015.11.09-11).

8. **P. Ayria**, A. R. T. Nugraha, S. Tanaka, R. Saito, Indirect transition ARPES in graphene, FNTG 50 (2016.02.20-22).

Bibliography

[1] K. S. Novoselov, A. K. Geim, S. V. Morozov, D. Jiang, M. I. Katsnelson, I. V. Grigorieva, S. V. Dubonos, and A. A. Firsov, Science **306**, 666–669 (2004).

[2] K. S. Novoselov, A. K. Geim, S. V. Morozov, D. Jiang, M. I. Katsnelson, I. V. Grigorieva, S. V. Dubonos, and A. A. Firsov, Nature **438**, 197–200 (2005).

[3] A. Bostwick T. Ohta, T. Seyller, K. Horn, and E. Rotenberg, science **313**, 951 (2006).

[4] A. K. Geim, Science **324**, 1530–1534 (2009).

[5] A. H. MacDonald and R. Bistritzer, Nature **474**, 453–454 (2011).

[6] A. Damascelli, Z. Hussain, and Z. X. Shen, Rev. Mod. Phys. **75**, 473 (2003).

[7] M. Mucha-Kruczyński, O. Tsyplyatyev, A. Grishin, E. McCann, V. I. Fal'ko, A. Bostwick, and E. Rotenberg, Phys. Rev. B **77**, 195403 (2008).

[8] Y. Liu, G. Bian, T. Miller, and T.-C. Chiang, Phys. Rev. Lett. **107**, 166803 (2011).

[9] C. Hwang, C.-H. Park, A. D. Siegel, A. V. Fedorov, S. G. Louie, and A. Lanzara, Phys. Rev. B **84**, 125422 (2011).

[10] I. Gierz, J. Henk, H. Höchst, C.R Ast, and Kern K., Phys. Rev. B **83**, 121408 (2011).

[11] Y. Liu, Longxiang Zhang, M. K. Brinkley, G. Bian, T. Miller, and T.-C. Chiang, Phys. Rev. Lett. **105**, 136804 (2010).

[12] Shin-ichiro Tanaka, Masaharu Matsunami, and Shin-ichi Kimura, Scientific reports **3** (2013).

[13] P. Ayria, A. R. T. Nugraha, E.H. Hasdeo, T. R. Czank, S. Tanaka, and R. Saito, Phys. Rev. B **92**, 195148 (2015).

[14] S. Hufner. Photoelectron Spectroscopy. Springer, (1996).

[15] Lothar Ley Manuel Cardona. Photoemission in solids: General principles. Springer-Verlag, (1987).

[16] A. Sekiyama S. Suga. Photoelectron Spectroscopy Bulk and Surface Electronic Structure. Springer, 2014.

[17] Jim J. Napolitano J. J. Sakurai. Modern Quantum Mechanics. Addison-Wesley, (1994).

[18] S Tanuma, CJ Powell, and DR Penn, Surface and Interface Analysis **43**(3), 689–713 (2011).

[19] CR Brundle, Journal of Vacuum Science & Technology **11**(1), 212–224 (1974).

[20] H. Wadati, A. Chikamatsu, M. Takizawa, R. Hashimoto, H. Kumigashira, T. Yoshida, T. Mizokawa, A. Fujimori, M. Oshima, M. Lippmaa, M. Kawasaki, and H. Koinuma, Phys. Rev. B **74**, 115114 (Sep 2006).

[21] Thomas James Kleeman. "Rb- K- intercalated bilayer graphene studied by high-resolution ARPES". Master's thesis, Tohoku University, (2012).

[22] H. Luth. Surface and Interfaces of Solid Materials. Springer, 1995.

[23] A. Grüneis, R. Saito, Ge. G. Samsonidze, T. Kimura, M. A. Pimenta, A. Jorio, A. G. Souza Filho, G. Dresselhaus, and M. S. Dresselhaus, Phys. Rev. B **67**, 165402 (2003).

[24] I. Gierz, M. Lindroos, H. Höchst, C. R. Ast, and Klaus Kern, nano Lett. **12(8)**, 3900 (2012).

[25] G. Malmstrom and J. Rundgren, J.Phys.C: Solid State Physics **13**, L61 (1980).

[26] S. Y. Zhou, D. A. Siegel, A. V. Fedorov, and A. Lanzara, Phys. Rev. B **78**, 193404 (Nov 2008).

[27] T. Seyller K. Horn A. Bostwick, T. Ohta and E. Rotenberg, Nat. Phys. **3**, 36 (2007).

[28] M. Calandra and F. Mauri, Phys. Rev. B **76**, 205411 (2007).

[29] W-K Tse and S. Das Sarma, Phys. Rev. Lett. **99**, 236802 (2007).

[30] Gerald D. Mahan. Many-particle physics. Springer Science & Business Media, (2000).

[31] G. Grimvall. Electron-phonon interaction in metals. North-Holland, (1980).

[32] P.Giannozzi et. al, Journal of Physics: Condensed Matter **21**, 395502 (19pp) (2009).

[33] Jeil Jung and Allan H. MacDonald, Phys. Rev. B **87**, 195450 (May 2013).

[34] Pierre Delhaes. Graphite and Precursors. Science, (2000).

[35] R. Nicklow, N. Wakabayashi, and H. G. Smith, Phys. Rev. B **5**, 4951–4962 (Jun 1972).

[36] R.A. Jishi, L. Venkataraman, M.S. Dresselhaus, and G. Dresselhaus, Chem. Phys. Lett. **209**, 77–82 (1993).

[37] T. Aizawa, R. Souda, S. Otani, Y. Ishizawa, and C. Oshima, Phys. Rev. B **42**, 11469–11478 (Dec 1990).

[38] S. Siebentritt, R. Pues, K.-H. Rieder, and A. M. Shikin, Phys. Rev. B **55**, 7927–7934 (1997).

[39] J. Maultzsch, S. Reich, C. Thomsen, H. Requardt, and P. Ordejón, Phys. Rev. Lett. **92**, 075501 (Feb 2004).

[40] G. D. Mahan, Phys. Rev. B **65**, 235402 (2002).

[41] R. Saito, G. Dresselhaus, and M. S. Dresselhaus, *Physical Properties of Carbon Nanotubes* (Imperial College Press, London, 1998).

[42] R. A. Jishi, M. S. Dresselhaus, G. Dresselhaus, K. Wang, P. Zhou, A. M. Rao, and P. C. Eklund, Chem. Phys. Lett. **206**, 187 (1993).

[43] G. D. Mahan and Gun Sang Jeon, Phys. Rev. B **70**, 075405 (2004).

[44] Gun Sang Jeon and G. D. Mahan, Phys. Rev. B **72**, 155415 (2005).

[45] O. Dubay and G. Kresse, Phys. Rev. B **67**, 035401 (2003).

[46] Lin-Hui Ye, Bang-Gui Liu, Ding-Sheng Wang, and Rushan Han, Phys. Rev. B **69**, 235409 (2004).

[47] Roland Gillen, Marcel Mohr, Christian Thomsen, and Janina Maultzsch, Phys. Rev. B **80**(15), 155418 (2009).

[48] Nicolas Mounet and Nicola Marzari, Phys. Rev. B **71**(20), 205214 (May 2005).

[49] MS Dresselhaus, G Dresselhaus, PC Eklund, and DDL Chung, Materials Science and Engineering **31**, 141–152 (1977).

[50] M. Mohr, J. Maultzsch, E. Dobardzic, S. Reich, I. Milosevic, M. Damnjanovic, A. Bosak, M. Krisch, and C. Thomsen, Phys. Rev. B **76**, 035439 (2007).

[51] Fernando de Juan, Antonio Politano, Gennaro Chiarello, and Herbert A Fertig, Carbon **85**, 225–232 (2015).

[52] M. Born and E. Wolf. Principles of Optics. Pergamon, Oxford, 1970.

[53] R. Matzdorf A. Gerlach and A. Goldmann, Phys.Rev.B **58**, 10969 (1998).

[54] A. Gerlach A. Goldmann F. Pforte, T. Michalke and R. Matzdorf, Phys. Rev. B **63**, 115405 (2001).

[55] M. T. Chowdhury R. Saito, M. S. Dresselhaus, Phys. Rev. B **85**, 115410 (2012).

[56] E. L. Shirley, L. J. Terminello, A. Santoni, and F. J. Himpsel, Phys. Rev. B **51**, 13614 (1995).

[57] G. Brocks V. M. Karpan J. van den Brink G. Giovannetti, P. A. Khomyakov and P. J. Kelly, Phys. Rev. Lett. **101**, 026803 (2008).

[58] C. Hamaguchi. Basic semicondutor physics. Springer, 2001.

[59] B. K. Ridley FRS. Quantum Processes in semiconductors. OXFORD, (2013).

[60] Orest J. Glembocki and Fred H. Pollak, Phys. Rev. Lett. **48**, 413–416 (Feb 1982).

[61] J Jiang, R Saito, A Grüneis, G Dresselhaus, and MS Dresselhaus, Chemical physics letters **392**(4), 383–389 (2004).

[62] J. Jiang, R. Saito, Ge. G. Samsonidze, S. G. Chou, A. Jorio, G. Dresselhaus, and M. S. Dresselhaus, Phys. Rev. B **72**, 235408 (2005).

[63] J. Jiang, R. Saito, Ge. G. Samsonidze, S. G. Chou, A. Jorio, G. Dresselhaus, and M. S. Dresselhaus, Phys. Rev. B **72**, 235408 (2005).

[64] Gerald D. Mahan, , 2000).

[65] D. L. Mafra M. S. C. Mazzoni L. M. Malard, M. H. D. Guimarães and A. Jorio, Phys. Rev. B **79**, 125426 (2009).

[66] V. M. Silkin E. E. Krasovskii E. Kogan, V. U. Nazarov, Arxiv page 1306.4084 (2013).

[67] E. Kogan and V. U. Nazarov, Phys. Rev. B **85**, 115418 (2012).

[68] A. Jorio M. S. Dresselhaus, G. Dresselhaus. Group Theory: Application to the Physics of Condensed Matter. Springer, (2008).

[69] Krishnakumar S.R. Menon S.K. Mahatha, surface Science **606**, 1705–1708 (2012).

[70] V. M. Silkin, J. Zhao, F. Guinea, E. V. Chulkov, P. M. Echenique, and H. Petek, Phys. Rev. B **80**, 121408 (Sep 2009).

[71] E. Kogan, V. U. Nazarov, V. M. Silkin, and M. Kaveh, Phys. Rev. B **89**, 165430 (Apr 2014).

[72] S. Reich and C. Thomsen, Philos. Trans. Roy. Soc. **362**, 2271–2288 (2004).

[73] Dipl. Phys. J. Maultzsch C. Thomsen, Dr. S. Reich. Carbon Nanotubes: Basic Concepts and Physical Properties. Wiley, (2007).

[74] J. Berkowitz. Photoabsorption, Photoionization, and Photoelectron Spectroscopy, 1979.

[75] Ge. G. Samsonidze, E. B. Barros, R. Saito, J. Jiang, G. Dresselhaus, and M. S. Dresselhaus, Phys. Rev. B **75**, 155420 (2007).

[76] Kentaro Sato, Jin Sung Park, Riichiro Saito, Chunxiao Cong, Ting Yu, Chun Hung Lui, Tony F. Heinz, Gene Dresselhaus, and Mildred S. Dresselhaus, Phys. Rev. B **84**, 035419 (July 2011).

[77] Michele Lazzeri, Claudio Attaccalite, Ludger Wirtz, and Francesco Mauri, Phys. Rev. B **78**, 081406 (Aug 2008).

[78] A. G. Marinopoulos, Lucia Reining, Angel Rubio, and Valerio Olevano, Phys. Rev. B **69**, 245419 (Jun 2004).

[79] T. O. Wehling, I. Grigorenko, A. I. Lichtenstein, and A. V. Balatsky, Phys. Rev. Lett. **101**, 216803 (Nov 2008).

[80] Yuanbo Zhang, Victor W Brar, Feng Wang, Caglar Girit, Yossi Yayon, Melissa Panlasigui, Alex Zettl, and Michael F Crommie, Nature Physics **4**(8), 627–630 (2008).

[81] K. M. Borysenko, J. T. Mullen, E. A. Barry, S. Paul, Y. G. Semenov, J. M. Zavada, M. Buongiorno Nardelli, and K. W. Kim, Phys. Rev. B **81**, 121412 (2010).